Characterization of RF Signal Coupling into MeerKAT Telescopes

by

Stanley Okoth **Kuja**

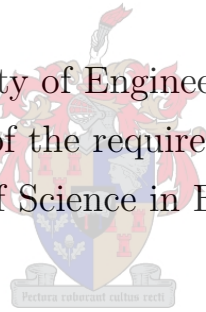

Thesis presented to the Faculty of Engineering, Stellenbosch University
in partial fulfilment of the requirements for the degree
of Master of Science in Engineering

Department of Electrical and Electronic Engineering,
Stellenbosch University

Supervisor: Dr. Pieter Gideon Wiid

December 2015

Declaration

I declare that the entirety of the work contained in this thesis is my own original work and that I have not previously in its entirety or in part submitted it for obtaining a qualification in any other university. No part of this research may be reproduced without prior knowledge of the author and Stellenbosch University.

Date: September 2015

Abstract

The study of weaker astronomical waves originating from billions of light years away could give an insight into the dawn of the universe's history. This requires the use of highly sensitive radio receivers and large radio telescopes for the detection of such mysterious signals. The MeerKAT facility will form part of the square kilometre array (SKA) which will have orders of magnitude greater sensitivity than existing radio telescopes. However, radio frequency interference (RFI) becomes a concomitant worry to such sensitive equipment.

The proximity of adjacent structures of the MeerKAT dishes at the core area, provides a possibility of a high inter–coupling problem between the nearby dishes, even from low–level emissions due to currents on structure cables. This thesis focuses on the electromagnetic (EM) characterization of a single dish using a physical scale model and computational electromagnetic (CEM) modelling. Together with field measurements, the verified CEM model can be used for further investigations into coupling between MeerKAT antennas. The South African SKA has ensured that care is taken in the shielding design of critical areas on the MeerKAT structure including the receiver indexer (RI) and cable entry point (stub–up). Due to the extreme sensitivity of the project, we qualify the shielding effectiveness with computational and scale modelling and on–site radio frequency (RF) coupling investigations on the MeerKAT dish structures.

The CEM code FEKO and method of moments frequency domain numerical technique is utilised throughout the study. The FEKO model verification is successfully achieved through measurement of a physical scale model in an anechoic chamber. The validated CEM model is confidently used to complement field measurements. A good correlation is attained between measurement and simulation through the transfer function determined from an incident electric field and the associated coupled currents on different cables that route to the RI and the earth cable at the stub–up region.

The verified CEM model can now be used for dish to dish coupling studies which will predict the nature of EM environment at the core site and lead to possible recommendations before the full commissioning of the entire array of MeerKAT antennas.

Opsomming

Die studie van swakker astronomiese golwe afkomstig van biljoene ligjare weg kan insig gee aan die begin van die heelal se geskiedenis. Om hierdie geheimsinnige seine op te tel benodig die gebruik van hoogs sensitiewe radio ontvangers en groot radio teleskope. Die MeerKAT fasiliteit sal deel vorm van die Square Kilometer Array (SKA) wat ordes meer sensitiwiteit as enige bestaande radio teleskoop sal hê. Radiofrekwensie–steuring is egter 'n gepaardgaande bekommernis met sensitiewe toerusting van hierdie aard.

Die nabyheid van die aangrensende strukture in die kern–area van die MeerKAT skottels bied 'n moontlikheid van hoë interkoppeling probleme aan tussen die nabygeleë skottels, wat selfs veroorsaak word deur lae–vlak emissie as gevolg van strome op die kabels van die struktuur. Hierdie tesis fokus op die elektromagnetiese (EM) karakterisering van 'n enkele skottel met behulp van 'n fisiese skaalmodel en elektromagnetiese modellering deur rekenaar sagteware. Saam met die veld–metings kan die geverifieerde sagteware–model gebruik word om verdere ondersoek in te stel oor die koppeling tussen die MeerKAT antennas. Die Suid–Afrikaanse SKA het verseker dat sorg getref word in die afskerming ontwerp van kritieke areas van die MeerKAT struktuur, insluitend die ontvanger aanwyser en kabel intree punt. As gevolg van die uiterste sensitiwiteit van die projek, staaf ons die doeltreffendheid van die afskerming met sagteware en skaal–modellering, asook deur die ondersoek van die radiofrekwensie (RF) koppeling van die MeerKAT skottel strukture op die terrein self.

Die EM sagteware–kode FEKO en die frekwensie–domein numeriese tegniek genaamd metode van momente is aangewend regdeur hierdie studie. Verifikasie van die FEKO–model is suksesvol bereik deur die meting van 'n fisiese model in 'n anegoïese kamer. Die goedgekeurde EM sagteware–model is met selfvertroue gebruik om die veld–metings aan te vul. 'n Goeie korrelasie word bereik tussen meting en simulasie deur die oordragsfunksie, wat bepaal word vanaf 'n inkomende elektriese veld en die gepaardgaande gekoppelde strome op verskillende kabels. Hierdie kabels span na die ontvanger aanwyser en die gronddraad by die kabel intree gebied.

Die geverifieerde EM sagteware–model kan vorentoe gebruik word vir skottel–tot–skottel koppeling studies wat die aard van die EM–omgewing by die kern–terrain kan voorspel en lei tot moontlike aanbevelings voor die ingebruikneming van die hele opstelling van MeerKAT antennas.

Acknowledgements

I wish to express my deepest gratitude to my supervisor, Dr. Gideon Wiid, for his excellent leadership by being a good listener, patient, caring and offering the freedom to explore on my own while at the same time providing a clear direction where I faltered. Thank you for being very supportive on the technical aspects of my work as well as meticulous on grammar and the general flow of ideas within the dissertation. My appreciation goes to Prof. Howard Reader for the trust and the opportunity to join the field of EMC engineering. You are an academic doyen whom I admire his professionalism and your good sense of humour that always brought a smile upon my face.

I am grateful to my love, Iris, for her constant prayers, encouragement through hard times, with tons of love and patience. To my late parents (Mr. & Mrs. Kuja), I will forever be indebted to them for their love and instilling the virtue of hard–work and patience. I want to thank my uncle, Nyakado, for being a good role model, mentor, friend and best dad that one could ever desire in life; to you and the wife you are a blessing. Very special acknowledgement to my beautiful sisters (Zam, Tess and Rose), sisters–in–law (Joyce and Jackline), brothers and the extended family for their unwavering support throughout my study.

My thanks go to the following people for their numerous contribution to the work done on this dissertation: Anneke Bester, Stephan Combrink and Joely for helping with measurements. Carel Van der Merwe and Niko Kriek for assisting with measurement campaign arrangements. Wessel Croukamp for workshop technical support. Danie Ludick for help in accessing the Centre for High Performance Computing (CHPC) in Cape Town, South Africa. Andre Young for orientation on the use of university's computational facility (Babbage). Mariet Venter for the translation of my abstract to Afrikan version. TJ for his generous time he spent in perusing through the manuscript to offer valuable comments that helped improve the document. The entire EMRIN group (Gideon, Stephan, Hardie, Joely and TJ) for the constructive discussions during our regular group meetings and the friendly environment you provided in room 212 E.

My gratitude extend to my best friend Mathews Opondo for his constant support and inspiration. Thank you Reagan, Brian, Lincoln, Easter, Amondi, Enock, Boiyo, Ang'anyo and the family for your prayers and encouragement. To Dr. Joely and TJ thank you for always cheering me on and especially to Joely for the swimming and football sessions you actively engage me in. Finally, to all my friends may God bless you for playing an active role in my life.

Dedication

He is the God who makes me strong, who makes my pathway safe —Psalm 18:32 (GNT)

—To Him I dedicate this dissertation —

Contents

List of Figures

List of Tables

Nomenclature

Symbols and Units

η	Antenna Efficiency	dB
λ	Wavelength	m
π	Pie	
A_{eff}	Effective Aperture Area	m^2
AF	Antenna Factor	m^{-1}
B	Observation Bandwidth	Hz
c	Speed of Light	ms^{-1}
D	Antenna Directivity	
E	Electric Field	Vm^{-1}
f	Frequency	Hz
G	Antenna Gain	dB
I	Linear Current	A
k	Boltzmann's Constant	JK^{-1}
P	Power	W
R	Distance	m
S	Receiver Sensitivity	$Wm^{-2}Hz^{-1}$
S_{avg}	Power Density	Wm^{-2}
T	Temperature	K
t	Integration Time	s
TF	Transfer Function	$dB\mu\Omega m^{-1}$

V	Voltage	V

Abbreviations

AUT	Antenna Under Test
CM	Common Mode
COTS	Commercial Off–the–Shelf
DME	Distance Measuring Equipment
DOA	Direction–Of–Arrival
DUT	Device Under Test
EM	Electromagnetic
EMC	Electromagnetic Compatibility
EMRIN	EMC Metrology Research and Innovation
ERS	Emission Reference Source
FFT	Fast Fourier Transform
FSPL	Free Space Path Loss
GLONASS	Global Navigation Satellite System
GPS	Global Positioning System
GR	Ground Reflections
HPBW	Half Power Beam–Width
ICASA	Independent Communication Authority of South Africa
IF	Intermediate Frequency
ITU	International Telecommunications Union
LHCP	Left–Hand Circular Polarization
LNA	Low Noise Amplifier
LO	Local Oscillator
LOFAR	Lower–Frequency Array
LPDA	Log–Periodic Dipole Antenna
OATS	Open Area Test Site
PEC	Perfect Electric Conductor
PSD	Power Spectral Density
RF	Radio Frequency
RFI	Radio Frequency Interference
RHCP	Right–Hand Circular Polarization
SABRE	South African Frequency Band Re–Planning Exercise

SDC	Shielded Drive Compartment
SIS	Superconductor–Insulator–Superconductor
SK	Spectral Kurtosis
SKA	Square Kilometre Array
SOI	Signal–Of–Interest
VLBA	Very Long Baseline Aperture–synthesis
VLBI	Very Large Baseline Interferometry
VNA	Vector Network Analyser

CHAPTER 1

Introduction

From the early stages of human knowledge until the modern technological era, scientists seek to answer the following fundamental questions: How are Galaxies formed? How did the universe in which we inhabit come to existence, has it really transformed and how, and what would be its final destiny? In order to find answers to these questions and to develop new laws of nature, or to uphold the current ones, scientists yearn to conduct deep–space observations using sophisticated equipment. In the past, surveys were exclusively carried out in the visible light range using "optical telescopes", however this changed dramatically in the year 1932. It is a time that can be regarded as the beginning of a new epoch in radio astronomy.

The first radio map of the skies was produced by Reber, an amateur, who had been intrigued by Jansky's observations of the milky way in 1932, and was published in 1942 [1]. Since then radio telescopes have developed to the point where there are two main types. There are large single dish telescopes (such as Arecibo [1]), and arrays of smaller dishes such as the Low–Frequency Array (LOFAR), which has recently become fully operational [2, 3]. These telescopes make two different types of observations: active; which utilizes RADAR technology, and passive; which pick up radio waves emitted by astronomical sources. As radio telescopes become larger and more sensitive, further data on astronomical objects can be collected, leading to a much better understanding of the universe as a general concept. To this end the Square Kilometre Array (SKA) telescope has been commissioned.

The SKA project was first discussed in 1993, and since then has grown into a global project, with the telescope dishes being set up in South Africa and Australia, in large remote areas of both countries [4].

1.1 The MeerKAT Telescope

The initial South African Square Kilometre Array (SKA) demonstrator known as Karoo Array Telescope Seven (KAT–7) was completed by 2010 and is now fully operational. The KAT–7 was a prototype used by South Africa to demonstrate its technology capabilities in bidding to host the SKA project. After a competitive bidding process, South Africa was given the offer to host 70 % of the telescopes. It then embarked on the construction of the second demonstrator; MeerKAT. It is an array of 64 dishes of Gregorian offset configuration. The SKA will be the worlds largest radio telescope, consisting of thousands of receivers; the MeerKAT is a precursor to this project and will become a part of the SKA at a later stage. The MeerKAT site is located within a radio quiet reserve established in the remote town of Carnavon in the Northern Cape Province of South Africa. The first dish (M63) was raised on the 27^{th} of March 2014 [5] and below is a photo of the dish (Figure 1.1 (b)) taken by the author at the Karoo site in July, 2014.

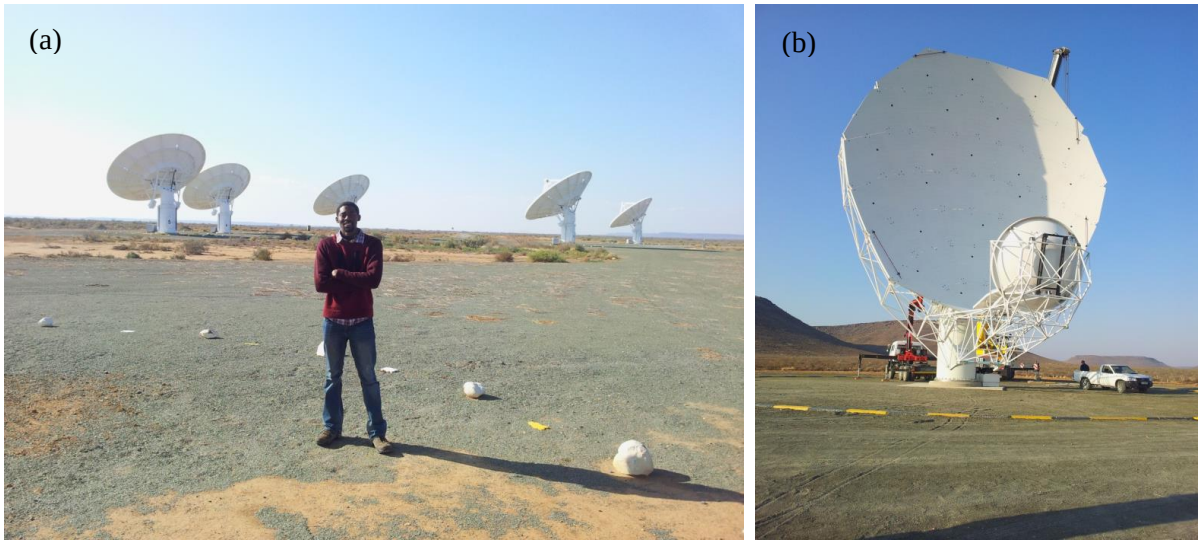

Figure 1.1: (a) Five of the KAT–7 dishes and (b) the MeerKAT (M63) at the core site

1.2 Noise and Interference (Engineering Perspective)

When dealing with electrical measurements, noise is any undesired electric voltage or current source that is present in the circuit and accompanies the desired signal. In general, its sources can be divided into three categories: a) the inherent noise sources generated by random variations within physical networks like thermal and Poisson noise; b) artificial noise sources such as switches, motors, computers, digital electronics and radio transmitting and receiving devices; and c) the induced or environmental noise due to natural disturbances such as lightning and solar activity. Interference is a disturbance that affects an electrical circuit due to noise and it can be eliminated. On the other hand, only the magnitude of the noise can be minimised (until it no longer generates interference) but it cannot be eliminated [6].

The ability of an electronic network to function dependably within an interference environment is known as electromagnetic compatibility (EMC) [6]. Therefore, appropriate EMC throughout the design stages is a primary concern for engineers. They ensure that an electronic network is able to operate effectively in its intended electromagnetic (EM) environment and does not generate interference to that environment. The EM environment is composed of both radiated (magnetic, electric or plane wave) and conducted (power or signal lines) energy [6].

There are two ways that EMC engineering can be approached: the crisis approach and the other is the systems approach [6]. In the former, the designer proceeds by completely ignoring EMC till the end of a working model, and testing–or in the worst case–experiences in the field indicate that there is a problem. The disadvantage of this approach is that, the solutions are usually implemented at late stages of the model, which makes it very expensive and comprise undesirable "add ons." In the latter approach, EMC is considered throughout the planning phases where the engineer anticipates EMC problems at the outset of the design process. An attempt is made to find the remaining problems in the early prototype stages and the final prototypes are tested for EMC as thoroughly as possible. Therefore, EMC becomes an integral part of the electrical and mechanical design of the finished product. Also, we can say that EMC is designed into–and not added onto–the product. This approach is found to be the most desirable and cost effective as well. The South African SKA opted for the latter. The development of MeerKAT is taking place in stages to optimise design and minimise risks at each stage. In this respect, our EMC Metrology Research and Innovation (EMRIN) group from Stellenbosch University has been actively involved in the EMC metrology issues for the SKA.

1.3 Astronomical signals and RFI

Radio frequency interference (RFI) refers to all undesired signals in the radio spectrum. This can infiltrate a radio telescope and interfere with the astronomical signals that are many factors of ten below the noise floor of the receiving system. Thus, the power level at which the RFI begins to be harmful is far lower for radio astronomy than it is for other radio communication services. The variety of potential RFI sources, therefore, is very large. A clear separation is necessary for scientific observations and scientists have developed different RFI mitigation algorithms. However, management of RFI emissions takes precedence over RFI mitigation in the signal path [7]. And since radio observatories significantly generate harmful emissions, the research focuses on the characterization of these self–generated radio frequency (RF) signals on the MeerKAT telescopes. The sensitivity of a single radio astronomy observation can be defined as [8]:

$$\frac{\Delta P}{P} = \frac{1}{\sqrt{f_0 t}} \tag{1.1}$$

where ΔP and P are power spectral density of the noise, Δf_0 and t are the bandwidth and integration time respectively. From the above equation, it can be seen that more sensitive observations are made when the bandwidth is wider. Consequently, astronomers are experiencing continuous interference problem in the recent years, as RF bandwidth has become growingly inadequate.

1.4 Observation Methods

Radio astronomy survey techniques can be categorized into four classes: Continuum, spectral line, solar and interferometric observations. The first three approaches can be used with a single telescope, while the fourth requires an array of telescope dishes. Since the SKA is composed of an array of antennas, only the interferometric observation is briefly discussed.

Interferometry

The use of two or more telescopes is called arraying. In radio interferometry, greater angular resolution of the radio image is attained when various telescope dishes concurrently scan the same celestial body. The distance between any two radio antennas can be extremely

Figure 1.2: The SKA map of the MeerKAT core from the air [5]

large, for instance in Very Large Baseline Interferometry (VLBI) where the antennas are situated in different continents. The data that is gathered from the multiple sensors (antennas) is combined and correlated in a central station, where all the geometrical delays and timing errors between the observatories are corrected through synchronization of the data. However, for the MeerKAT telescopes at the Karoo:

- The longest distance between any two receptors (the so–called maximum baseline) is 8 km and
- Forty eight of the MeerKAT receptors are concentrated in the core area which is approximately 500 m in radius (see Figure 1.2) [5].

Therefore, a high inter–coupling problem could potentially occur between the nearby telescopes at the core area, even from low–level radiations due to currents on structure cables. This thesis examines the techniques to characterize such EM wave propagation within the ambient environment of the MeerKAT systems.

1.5 Motivation and objectives

Radio frequency interference (RFI) has the potential to degrade the ability of the SKA telescopes to do the science for which they are being constructed. Therefore, the MeerKAT requires a pristine RFI environment in order to attain its scientific goals. And every effort has been made to maintain the EM quietness of South Africa's Karoo site thus far. A good understanding of the interference and propagation issues within the Karoo environment, with all its interconnected telescopes and planned arrays, is essential. The key problem here is that RFI is unwanted, but it already exists. This needs to be managed

with critical insight. The use of computational and physical models as well as on–site tests form part of a detailed understanding of coupling between, and interference into, MeerKAT systems. One key objective is to contribute to policies on determining safe zones and levels for electrical/ electronic activity, i.e. the nearby commercial off–the–shelf (COTS) equipment.

1.6 Thesis Outline

The organization of the thesis is as follows. Chapter 1 gives a brief background on the technological advancement in radio astronomy, the relevance of EMC metrology to SKA, the sensitivity of astronomical signals to RFI and the motivation and objectives of this research. In Chapter 2, a survey of relevant literature is presented and is dedicated to the review of radio astronomical telescopes and receivers, RFI in radio astronomy, techniques and equipment for monitoring RFI, layers of RFI mitigation and RFI characterization techniques in different environments. Chapter 3 describes FEKO as a simulation tool, the MeeKAT design of the scale models and the verification procedure for the computational model using the physical scale model. A detailed analysis of results and discussions of the research findings from on–site measurements and the verified FEKO model are given in chapter 4. Finally, the conclusions and recommendations on future work are presented in Chapter 5. At the end of every chapter, there is a summary of the most important points except in chapter 1. In addition, the dissertation contains appendixes A and B with supplemental information.

—Progress in science depends on new techniques, new discoveries and new ideas, probably in that order —

–Sydney Brenner –

CHAPTER 2

The Basics of Radio Astronomy and RFI

RESEARCH equipment used in radio astronomy have advanced considerably since the early days of Jansky and Reber [9]. Scientific observations are now being carried out in a much wider frequency range, from 30 MHz to 300 GHz. It is now feasible to construct and maintain more sensitive radio telescope receivers for scientific research, to observe far beyond our own Galaxy to the limits of the entire universe. Nonetheless, the presence of RFI may limit the capabilities of such instruments. This chapter documents the relevant theory pertaining to RFI mitigation techniques, radio astronomical telescopes and RFI characterization methods in different environments. It lays a foundation for the research discussions in subsequent chapters.

2.1 Radio Astronomical Telescopes

To increase sensitivity from far off celestial sources, the size of the radio telescopes need to remarkably increase. The diameter of the world's largest non–steerable radio telescope is 305 m, built in 1963 in Arecibo, Puerto Rico [10]. While that of the biggest fully steerable radio telescope is 100 m and it is situated in Green Bank, West Virginia (see Figure 2.1 next page) [10].

A typical radio telescope consists of a large parabolic antenna that collects and focuses very faint incoming radio waves on a detector called the feed antenna [10]. The detector

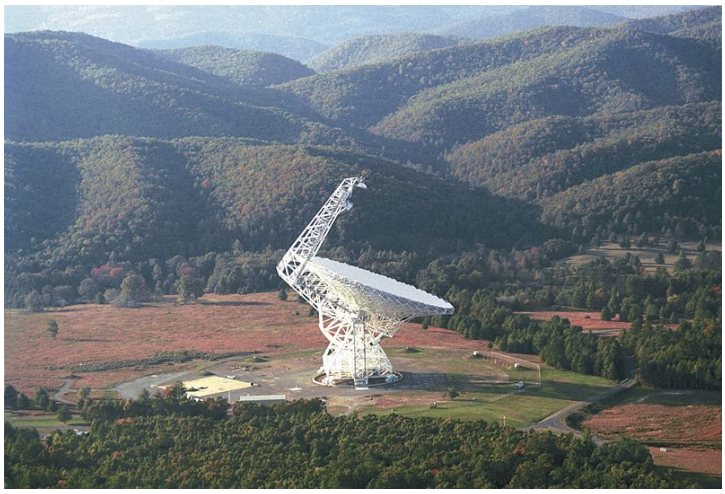

Figure 2.1: Green Bank 100 m diameter radio telescope

forms part of the receiver, which amplifies the signal and sends it to a computer for storage and analysis. The antenna is by far the most crucial component of any receiving system. Therefore, the design of this component and its proper selection is paramount. An antenna can be characterized according to the following parameters: radiation resistance, radiation pattern, beam–width and gain of its main lobe, position and magnitude of its side lobes, bandwidth, aperture, antenna correction factor and polarization of electric fields that it transmits or receives.

2.1.1 Radiation Resistance

If an antenna is considered as a load that terminates the feeder transmission line, it would have both a self impedance and mutual impedance. The self impedance is one that would be measured at the terminals of the antenna when it is in free space, whereas the mutual impedance is due to coupling between the antenna and the source. The self impedance is given by $Z_a = R_a + jX_a$, where R_a is the real antenna resistance accounting for the power absorbed and re–radiated by the antenna and X_a is the self–reactance. The real antenna resistance, $R_a = R_r + R_l$, where R_r is the radiation resistance and R_l is the loss ohmic resistance which contributes to the loss of efficiency of the antenna [11].

2.1.2 Radiation Pattern

The antenna radiation pattern is a graphical representation of the geometrical distribution of the radiated power over all space. It is typically expressed in the spherical coordinates as a function of space coordinates and is independent of distance.

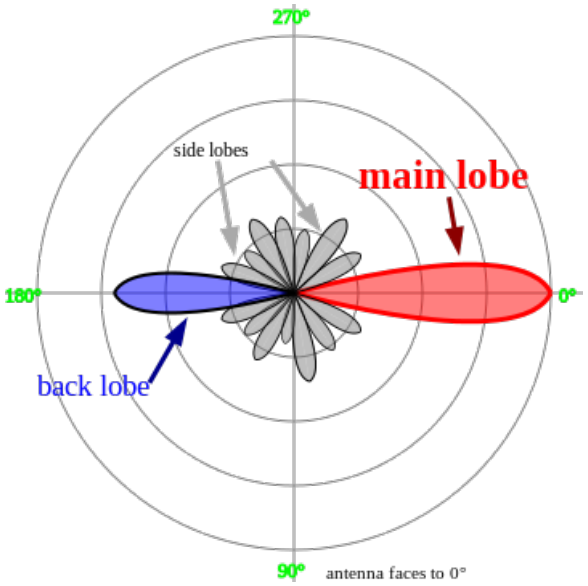

Figure 2.2: Antenna radiation pattern with the main, back and side lobes.

A radiation pattern usually consists of a main beam, one or a few near side lobes adjacent to the main beam and many far side lobes further away from the main beam (Figure 2.2). The main beam can be of various shapes, e.g., toroidal, pencil, or elliptical beam. The near side lobes usually have predictable power levels and directions. The far side lobes are very random in their power levels and directions, but generally the power levels decrease rapidly and level off at a threshold value. The randomness of the far side lobes depends on the detailed structure of the antenna, e.g., the accuracy of the surface, the shape of the edge, and the antenna supporting elements [12].

The patterns can be seriously affected by the environment. For instance, that of an antenna operating in the low frequency (30–300 kHz range) or medium frequency (300–3000 kHz range) band and installed above the ground is profoundly influenced by the lossy earth. Or, the radiation pattern of an antenna installed on–board a ship or an air–plane is distorted by the metallic structure in its surrounding.

The radiated power is at its maximum along its bore–sight which is usually plotted at zero degrees. At this position, most of the power is concentrated in the main lobe. When the power is radiated uniformly in all direction, an $omni-directional$ pattern is achieved and if this power is uniform, *isotropic* radiation is obtained. In order to achieve uniform radiation in all directions, the isotropic radiator would have to be a point source. The pattern provides such useful information as the beam–width, directivity, gain, position of nulls and front to back ratio.

2.1.3 The Position and Magnitude of the Antenna Side Lobes

From the previous subsection and in particular in Figure 2.2, the radiation pattern has a main beam of radiation together with a back lobe and numerous side lobes [11]. The position and magnitude of the side lobes can accurately be calculated using spectral analysis theory. It is a critical and important characteristic in RF system design. Most RF designs aim to reduce or totally suppress such side lobes [13]. This is due to a desire, by the frequency planning authorities, to conserve natural resources such as bandwidth and to enable the radio frequency spectrum to be shared amongst many users. The frequency planning authorities sometimes dictate what the threshold level of side lobes should be and impose hefty fines on defaulters. For this reason, side lobes are an unwanted *nightmare* to RF system designers. The magnitude of the back lobe with respect to the main beam defines the front–to–back ratio which is a measure of the ability of the antenna to focus the beam in the desired forward direction [14].

Antenna Response Pattern

Unwanted signals during observations mostly leak through the side lobes of the antenna pattern, therefore the main beam response to these signals may be ignored. Recommendation in [15] gives a side lobe model for large reflector antennas operating in the frequency range of 2 to 30 GHz. It is a standard estimate of the response of many radio astronomy antennas. Also in the model, the magnitude of the side lobe level reduces with angular distance (in degrees) from the axis of the main beam and is equal to 32–25 logφ (dBi) for 1^o<φ <48^o (Figure 2.3). The impact of these undesired signals obviously depend on the angle of incidence relative to the axis of the main beam of the antenna, since the side lobe gain, as given by the model, varies from 32 to 10 dBi as a function of this angle. However, it is effective to determine the threshold levels of interference strength for a certain value of side lobe gain, which is chosen as 0 dBi. From this configuration, this side lobe level occurs at an angle of 19.05^o off the axis of the main beam. Therefore, a signal at the harmful threshold level defined for 0 dBi side lobe gain will surpass the criterion for the harmful level at the receiver input if it is incident at the antenna at an angle of less than 19.05^o [8].

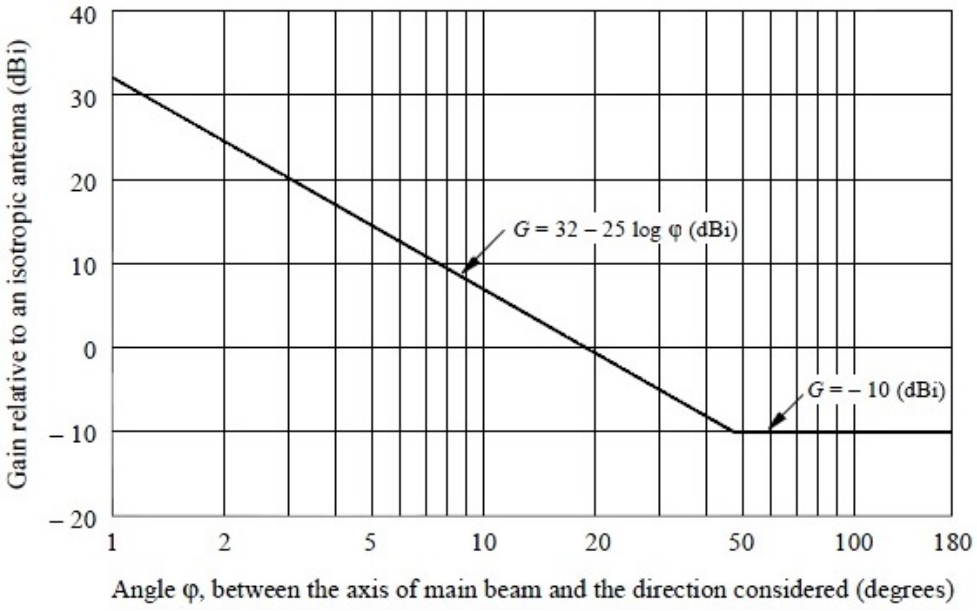

Figure 2.3: Reference radiation diagram showing the magnitude of the side lobe level as a function of angular distance in degrees [15].

2.1.4 Beam–width and Gain of an Antenna

The half power beam–width (HPBW), ϕ_{bw}, or beam–width, is the angle between the two directions of a two–dimensional radiation pattern at which the power gains are one–half of the peak gain. A toroidal beam or a circular torch beam has a single ϕ_{bw} parameter, and an elliptically shaped torch beam has two ϕ_{bw} parameters. Its value depends on the shape of the reflector and the method of illumination, among other factors [12]. A sketch of an antenna radiation pattern, its main–beam, and ϕ_{bw} is shown in Figure 2.4.

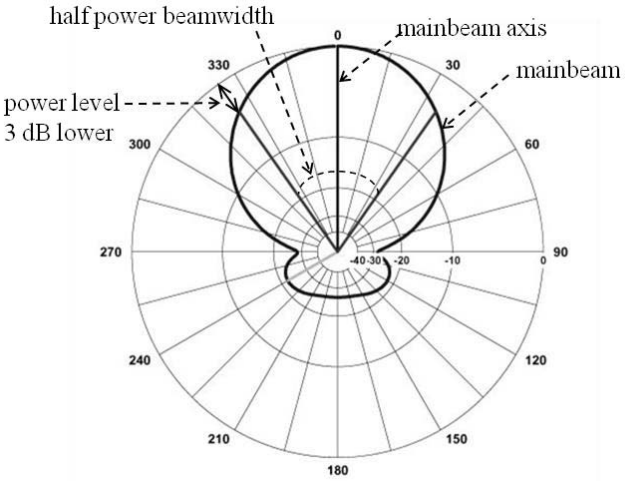

Figure 2.4: A sketch of antenna radiation pattern, antenna beam and half power beam–width (HPBW).

The gain of an antenna is defined as 4π times the ratio of the radiation intensity in a given direction to the total power radiated by the antenna. And it is calculated from the following formula:

$$G = \eta D \tag{2.1}$$

where η is the efficiency of the antenna (which normally vary between 50% and 90%) and D is the directivity which is the ratio of the maximum radiation from a lossless antenna to the average radiation from an isotropic antenna. The gain can be considered as a measure of the ability of the antenna to focus the energy into a smaller number of angles.

2.1.5 Bandwidth

Bandwidth can be defined as the range of usable frequencies which a signal occupies. Frequency usability refers to the power or voltage levels of the detected signal and is often taken at 50% or 70% respectively [16]. Although a range of frequencies is often quoted, bandwidth itself is an *absolute* value which is measured in hertz (Hz). The relation below defines bandwidth in percentage form:

$$B = \frac{\Delta f}{f_c} \times 100\% \tag{2.2}$$

where Δf is the frequency range in which the signal's spectral density is non–zero or above a small threshold value and f_c is the centre frequency in the band. Antennas operate efficiently and exhibit optimum performance at frequency ranges for which they are designed. Outside these frequency ranges, the signal may be degraded or completely undetectable.

2.1.6 Antenna Aperture

The aperture size of the antenna is related to its beam–width and gain. The larger the aperture, the narrower the beam–width and the higher the gain for any given frequency [11]. The magnitude of the effective aperture is sometimes expressed in terms of wavelengths: This is the case for narrowband or single frequency signals. However, for broadband applications, the physical dimensions may not resemble the wavelengths of operation. The effective aperture, A_{eff}, wavelength, λ and gain, G, of the antenna are related by the following mathematical expression:

$$G = \frac{4\pi A_{eff}}{\lambda^2} \tag{2.3}$$

This equation illustrates an important point, that is, the larger the effective area of an antenna, the larger the gain. By substituting $\lambda = \frac{c}{f}$, the above equation becomes:

$$G = \frac{4\pi A_{eff} f^2}{c^2} \tag{2.4}$$

where c is the speed of light. This equation defines the gain of an antenna as a function of frequency. If the gain of the antenna is held constant, the equation shows that the effective area, A_{eff}, decreases with increasing frequency and vice–versa. From the above equations, one can argue that in the design of RFI systems, a frequency range, say, 80 MHz to 1 GHz is a much physically large antenna than a frequency range from 900 MHz to 26 GHz. Therefore, low frequency measurements require huge reflectors to attain a reasonable angular resolution.

2.1.7 Antenna Factor (AF)

The application of antenna factor (AF), is in electromagnetic interference (EMI) testing when making radiated electric field (E–field) strength measurements. The AF (units of m^{-1}) refers to a term or factor that is applied to the reading of the receiver so that the reading can be converted to the field strength in either volts per metre (electric field strength) or amperes per metre (magnetic field strength). In linear terms, it is the ratio of the incident E–field strength to the voltage, V (units: V or μV) induced across the terminals of the receiving antenna, $AF = \frac{E}{V}$. In a 50 Ω system, the antenna factor is related to the antenna gain, G and the wavelength λ via [17]:

$$AF = \frac{9.73}{\lambda\sqrt{G}} \tag{2.5}$$

In logarithmic (dB) units the antenna factor, AF is expressed as:

$$AF = 20log(f_{MHz}) - G_{dBi} - 29.79 \tag{2.6}$$

2.1.8 Polarization

The antenna polarization refers to the polarization of the far–field EM wave generated by the antenna, while the polarization of the EM wave refers to the polarization of the electric–field of the EM wave [12]. The EM wave can be linearly, circularly, or elliptically polarized. For a linearly polarized EM wave, the direction of its electric field is constant with respect to the direction of the wave propagation. For an elliptically polarized EM wave, the direction of its electric field rotates with respect to the direction of the wave propagation, and it can be either right–hand circular polarization (RHCP) or left–hand circular polarization (LHCP). Circular polarization is a special case of elliptical polarization where the major and minor axes of the rotation are the same.

In radio communications, linear polarization is designated according to the relationship of the polarization to the Earth, and is usually horizontal or vertical [12]. For the terrestrial radio services, a radio signal is horizontally polarized when its electric–field is parallel to the horizontal plane (or ground), and it is vertically polarized when its electric–field is perpendicular to the horizontal plane. For the space radio services, a radio signal is horizontally polarized when its electric–field is parallel to the equatorial plane (or the east–west direction), and it is vertically polarized when its electric–field is perpendicular to the equatorial plane (or the north–south direction).

Characteristics of a radio system's propagation environment and operation may dictate the selection of polarization. For instance, in the case of propagation environment, vertical polarization is the preferred choice for a terrestrial radio relay system or broadcasting system to counter the lossy characteristics of the ground. On the other hand, circular polarization is the preferred choice for a space system operating in frequency bands subject to Faraday rotation in the ionosphere. In the case of operation, circular polarization is the preferred choice for the mobile satellite systems because it is difficult to align the linear polarization of the mobile earth station terminals.

Co–Polarization and Cross–Polarization

When a radio signal has the same polarization as the antenna's designated polarization, the signal and the antenna are mutually *co-polarized*. When the radio signal has orthogonal polarization to the antenna's designated polarization, i.e., horizontal vs vertical or RHCP vs LHCP, the signal and the antenna are mutually *cross-polarized*.

While an antenna is designed with a specific polarization, the unavoidable imperfection of the antenna geometry and its mounting structures can cause the antenna to have

cross–polarization characteristics in its operations. Therefore, an antenna is always associated with a co–polarization radiation pattern and a cross–polarization radiation pattern, and it always transmits and receives cross–polarized radio signals. It is important that the co–polarization be larger than the cross–polarization in order to receive optimum power.

2.2 Friis Transmission Formula

Friis developed the radio link formula after being interested in the power transfer through free space between a transmitting and a receiving antenna which are a distance apart. At that time, he was working on a broadband microwave–radio–relay system for telephone transmission. Figure 2.5 is a general radio system link that can be used to understand and derive the formula. From [16], the general expression for the power density radiated by an arbitrary transmitting antenna at a distance, R, is given by:

$$S_{avg} = \frac{G_t P_t}{4\pi R^2} \quad \text{W/m}^2 \tag{2.7}$$

where P_t is the transmitted power and G_t is the gain of the transmitting antenna. When this power density is incident on the receiving antenna, the concept of effective aperture area, (as discussed in subsection 2.1.6) can be used to obtain the received power as:

$$P_r = A_e S_{avg} = \frac{G_t P_t A_e}{4\pi R^2} \quad \text{W} \tag{2.8}$$

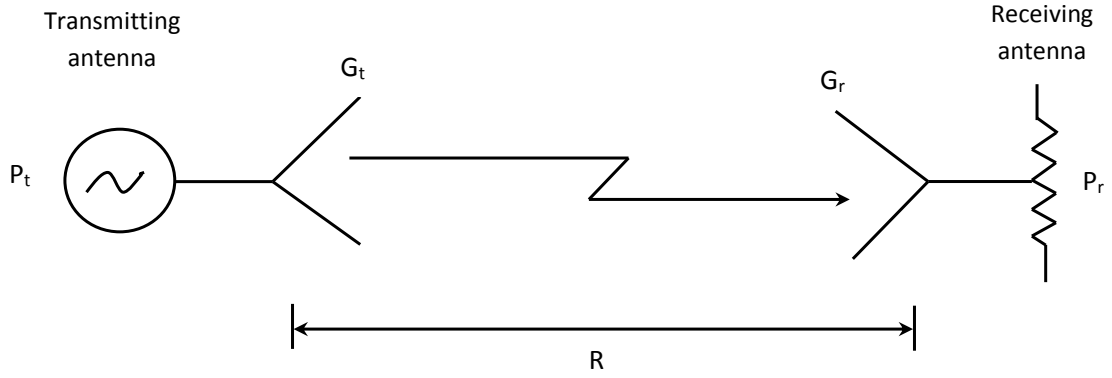

Figure 2.5: A basic free space radio system.

where A_e is the effective aperture area of the receiving antenna. Equation (2.3) is then utilized to relate the gain, G_r, of the receiving antenna and A_e. The final expression for the received power after appropriate substitution is done, is shown below.

$$P_r = \frac{G_t G_r \lambda^2}{(4\pi R)^2} P_t \text{ W} \tag{2.9}$$

This result is known as the *Friis transmission formula* and is very popular in wireless communications in addressing the important question of how much power is received by a radio antenna. The above equation shows that as the separation distance between the transmitter and receiver increases, the received power decreases as a function of $1/R^2$. This dependence is due to conservation of energy. And for very long distances, it appears to be prohibitively large, however, the space decay of $1/R^2$ is normally much better than the exponential decrease in power in wired communication links due to losses. The reason is that, power on the transmission line varies as a function of $e^{-2\alpha z}$, where α is the attenuation constant of the line, and at longer distances the exponential term decreases rapidly than the algebraic dependence of $1/R^2$ [16]. Therefore, for very long–distance communications, wireless radio links will perform better than wired links.

2.3 Radio Astronomical Receivers

The radio astronomical receiver is a radiometer used to measure the received power of electromagnetic radiation from celestial sources. The approaching signal is received through the antenna feed to the front–end low noise amplifier (LNA) via a transmission line, where the signal undergoes the initial stage of amplification [18]. The LNA is normally cryogenically cooled to minimise thermal noise [19]. A super–heterodyne radio telescope receiver uses frequency heterodyning for converting the RF signals to an intermediate frequency (IF) for additional amplification and processing. Further down–conversion of the IF signals to base–band is done for digitization purposes and thereafter, processed in the digital domain. Some of the modern receivers can perform direct RF digitization and down–conversion. Following the base–band conversion and digitization, a single dish telescope measures the total power in the observing band whereas array telescopes measure the correlated power between the pairs of antennas (baselines), in a manner similar to a correlation radiometer [18].

Figure 2.6 is a schematic illustration of a typical design of a super–heterodyne receiver system being used in high frequency data collection. The incoming RF signal, f_{RF}, is down–converted by the mixer and the local oscillator (LO) operating at f_{LO}. This results

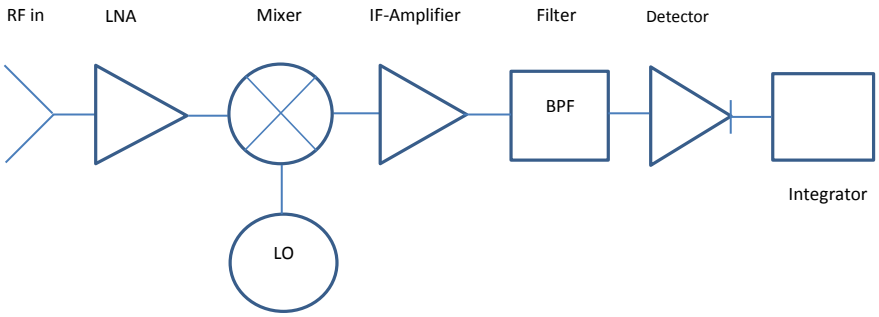

Figure 2.6: Schematic illustration of a super–heterodyne receiver system.

into an output IF signal, $f_{IF} = f_{RF} - f_{LO}$. Commonly, the mixer is a Schottky–diode or a superconductor–insulator–superconductor (SIS) unit. After the signal has been down–converted, then follows the second amplification of the signal at the IF section of the receiver before it is filtered and detected. The used demodulator is normally a square–law–detector and its function is to convert the changing IF signals to equivalent DC levels for the possibility of further data processing. Finally, an integrator is used to integrate the DC output signals for many seconds with the maximum integration time being set by the amplifier's stability and the Earth's rotation [20, 18]

Radio telescope receivers generate significant amounts of interference, whose impact in radio surveys should be nullified. The output signal is a mixture of the antenna temperature, T_A and the receiver temperature, T_r, as given by equation (2.10) below [18]:

$$P = kB(T_A + T_r) \tag{2.10}$$

where k is the Boltzmann's constant and B is the observation bandwidth.The above equation implies that the noise power, P, is actually the heating value of the signal and that a decrease in temperature or bandwidth leads to a corresponding decrease in noise power. Using an ideal integrator, the sensitivity of the receiver is defined by equation (2.11), where B_{lfn} is low frequency noise bandwidth and τ is the integration time [18].

$$\Delta T_{min} = \frac{T_A + T_r}{\sqrt{B_{lfn}\tau}} \tag{2.11}$$

The calibration of radio receivers before the survey sessions is essential. This is done by determining the levels of self–generated noise of the receiver, T_r, that is minimised at some stages during the signal processing. It is important to perform careful calibration

for the following reasons: If T_r is over–estimated, it reduces the threshold value and eventually lessens the sensitivity performance of the receiver. On the other hand, if T_r is under–estimated, the subsequent measurements will be skewed by the noise power of the receiver. When the receiver's components wear out, the associated self–generated noise can multiply, hence constant calibration is necessary. The most appropriate method used in calibrating a radio receiver is known as the Y–factor method [21]. In this approach, the receiver's noise figure is calculated by using two known noise sources, T_{hot} and T_{cold}. The advantage of this technique is that the receiver's gain and noise bandwidth do not need to be known. The Y–factor is calculated from the following equation.

$$Y = \frac{P_{hot}}{P_{cold}} = \frac{(T_r + T_{hot})kGB}{(T_r + T_{cold})kGB} = \frac{T_r + T_{hot}}{T_r + T_{cold}} \tag{2.12}$$

where G is the gain of the receiver, P_{hot} and P_{cold} are the noise powers obtained when the loads are connected to the device under test (DUT) and placed in a hot and cold environment respectively or basically switched ON and OFF, in which case the subscripts *hot* and *cold* are simply replaced with *on* and off as is the case in [22]. The receiver temperature, T_r, can be obtained from the previous equation as:

$$T_r = \frac{T_{hot} - YT_{cold}}{Y - 1} \tag{2.13}$$

The corresponding noise figure F_N is the amount of noise added to the output signal by the amplifier circuitry [21], and it should be nullified from the gathered data. The following equation can be used to calculate its value.

$$F_N = 10log(\frac{\frac{T_{hot}}{T_o} - 1}{Y - 1}) \tag{2.14}$$

where $T_o = 290^oK$ (Ambient temperature).

In general, strong RFI drives the receiver into its non–linear region and results in the production of artefacts which contaminate the output power spectrum, and eventually leads to undesirable effects in the radio images. For an array of antennas, where signals are received concurrently from various antenna elements and processed as baselines, the component of the astronomical source signal conducted by each of the antennas is mutually correlated. However, RFI being from a different line of sight, is not correlated as the astronomical signal. This reduces the impact of RFI in the scientific data. As the baseline length increases, the correlation of terrestrial RFI source is minimised and in the case of Very Long Baseline Interferometry (VLBI), the observations are mostly affected by

extraterrestrial (space–based) sources of interference rather than terrestrial sources.

2.4 Radio Frequency Interference

In ground–based scientific surveys, the RF spectrum is restricted by attenuation in the Earth's aerosphere. The existence of mobile electronic particles in the ionosphere makes the aerosphere opaque for radio signals below 30 MHz. As a result, they reflect the radio waves of this nature back to space. Also, gas molecules that deteriorate electromagnetic signals from space, set the upper limit in the ground–based observation and become notable beyond 300 GHz. Therefore, the restricted section of the RF spectrum is termed as the radio window. Another factor that limits the RF spectrum within the window is the man–made RFI. They are usually a multiple times stronger than the faint astronomical radio waves; consequently, they inhibit the radio spectrum appreciably. Radio telescopes are not only exposed to external RFI, but also to internal emissions too. In this section, different types of RFI sources and mitigation methods on the radio astronomical measurements are discussed. Also, frequency band allocation is presented, focusing on South Africa.

2.4.1 Allocation of Radio Frequency Bands in South Africa

Traditionally, the assigned band of frequencies in radio astronomy has been at the higher end of RF spectrum. A band of frequencies at the lower end of the spectrum was designated for commercial applications and usage by other sectors. However, industrialization and the accelerated growth in electronic, broadcasting and other related sectors led to an increased usage of frequencies designated for commercial use. Consequently, an over–crowding of the RF spectrum designated for commercial use occurred and the need for more frequencies became apparent. The *encroachment* on the RF spectrum allocated for radio astronomy meant that the band of spectrum which traditionally had been set aside for radio astronomy applications is now shared with other commercial applications [23]. An over–lap of the frequency bands is now evident and as a consequence, RF from nearby adjacent channels pose a constant threat to astronomical signals.

In addition, there is now move towards a society which requires that one accesses information at their fingertips *when they need it, where they need it, and in whatever format they need it*. As a result, more and more South Africans are becoming technologically savvy. Cellular telephony is no–longer the exclusive *toy* of the rich and famous, but has become a primary mode of communication (for both rich and poor) in urban and rural areas alike [24].

This proliferation of cellular telephony, WiFi and other bandwidth intensive devices and applications such as Facebook and Mxit has placed an upward pressure on the national telecommunications and broadcasting regulator (ICASA) [25].

Further evidence of increased frequency usage and consequent frequency clash is contained in the Independent Communication Authority of South Africa's (ICASA) endeavours known as SABRE–1 and SABRE–2. The South African Frequency Band Re–Planning Exercise (SABRE) was aimed primarily at re–allocation, migration of certain services and sharing of certain frequency bands. It arose out of the need for more frequency channels and an increased desire for more bandwidth usage [23, 26].

Table 2.1 on page 21 shows a summary of the spectrum allocation in South Africa for the band 30–1427 MHz. Only the frequencies for the major allocations are shown. The table shows how the entire HF/ VHF/ UHF bands have been proliferated by various commercial or industrial applications. It confirms the fact that not much spectrum allocation has been set aside for radio astronomy applications within these bands.

2.4.2 Radio Frequency Interference in Radio Astronomy

There are two main classes of radio frequency interference (RFI): external and internal RFI. The external interferences are generated due to various radio emissions within the surrounding environment. The radio ecology environment at radio observatories is made up of persistent interferences such as radio and television broadcast transmitters and the transitory interferences such as aircraft radar and aviation radio networks. It is fairly easy to detect persistent interference from radio broadcasts and their impact on the measured data can be cancelled out by selecting an interference free band for the survey. However, transitory noises are a bit challenging to identify and nullify; and their effect on the measured data is strenuous to estimate. To eliminate or manage this kind of RFI, very intricate mitigation algorithms are required, which are presented in section 2.6.

Activities arising from the operation of the observatories themselves make them a remarkable cause of noise. Inside these structures there are various emitting devices like index motors, computers, hydrogen maser, microwave ovens, just to mention but a few. Similarly, internal interferences can either be persistent or transitory in their characteristic and their impact on the radio observations can be huge, because these detrimental radiators are installed within or near the observatory and the receiver. In this subsection, the commonly known internal and external interference sources are discussed.

Table 2.1: Allocation of radio frequency spectrum in South Africa: 30–1427 MHz. This table was extracted from *Part* 3 of [23].

Frequency Band (MHz)	**Main Allocations**
30.01–74.8	Mobile/ Fixed/ Amateur
74.5–75.2	Aeronautical Navigation
75.2–87.5	Mobile/ Fixed
87.5–108	FM Sound Broadcasting
108–137	Aeronautical Radio Navigation/ Aeronautical Mobile
137–138	Mobile–Satellite/ Meteorological–Satellite/ Space Operation
138–144	Mobile/ Fixed
144–146	Amateur/ Amateur–Satellite
146–148	Mobile/ Fixed
148–149.9	Mobile–Satellite (E–to–S)/ Mobile/ Fixed
149.9–150.05	Radio Navigation–Satellite/ Land Mobile–Satellite
150.05–174	Mobile/ Fixed/ Maritime Mobile
174–238	TV Broadcast Channel 4 to 11
238–246	Mobile/ Fixed
246–254	TV Broadcast Channel 13
254–328.6	Mobile/ Fixed
328.6–335.4	Aeronautical Radio Navigation
335.4–399.9	Mobile/ Fixed
399.9–400.5	Radio Navigation–Satellite/ Land Mobile–Satellite
400.5–400.15	Standard Frequency and Time Signal
400.15–401	Mobile–Satellite/ Meteorological–Satellite/ Space Research
401–406	Meteorological Aids/ Space Operation (S–to–E)
406–406.1	Mobile–Satellite (E–to–S)
406.1–430	Mobile/ Fixed
430–440	Amateur Radio Allocation
440–470	Mobile/ Fixed
470–854	TV Broadcasting Channels 21–68
854–862	Fixed
862–960	Mobile/ Fixed
960–1215	Aeronautical Radio Navigation (DME/ Secondary Surveillance)
1215–1240	Radio Navigation/ Radio–location/ Satellite (LPD)
1240–1260	Radio Navigation/ Radio–location/ Amateur (ATCR)
1260–1300	Radio–location/ Amateur (ATCR)
1300–1350	Aeronautical Radio Navigation (ATCR)
1350–1400	Fixed/ Mobile/ Radio–location
1400–1427	Radio Astronomy/ Space Research

2.4.2.1 External Radio Interference

Radio interference from outside can be categorized into ground based (terrestrial emitters) and space generated RFI like satellite transmissions. The high transmission power and closer localization often makes ground based RFI more harmful. Scientific surveys are not carried out with very low angles of elevation, usually not below 20^o. This is because the aerosphere highly weakens the signals at such elevations where it is most dense. Consequently, the threats from these RFI will most probably affect scientific measurements through the side lobe reception of the antenna pattern. Also, very intense radiations can infiltrate the shielding of the receiver cables and contaminate the received signal in the IF part of the receiver.

The most irritating RFI are those within the detected signal or close bands since they will force their way through the bandpass filter of the receiver. However, scientific observations are mostly performed in high frequency region of preserved frequency bands, where the signals are not vulnerable to man–made RFI. For the purposes of clean data from scientific surveys, the interference spectrum should be tracked in the receiver's signal and the IF band during the down–conversion process. A list of these terrestrial based RFI are found in Table 2.1, 30–1427 MHz band.

There is an ever increasing extraterrestrial (space generated) interference because of the increasing demand of satellite telecommunication and air traffic usage. In fact, various frequency bands for radio navigation and communication, distance measuring equipment (DME) and aircraft radars have been occupied by air traffic. Therefore, telescope dishes that have been installed within the active air traffic regions can be hugely affected by these radio disturbances. Transmissions from some of the largest satellite telecommunication services, such as the Global Positioning System (GPS), the Russian Federation Global Navigation Satellite System (GLONASS), Global star and Iridium present a remarkably troublesome nuisance to radio scientists. Unfortunately, their services are provided in all corners of the world from telecast to satellite phone usage; but radio quiet zones do not apply to electronics in space. These extraterrestrial RFI generate both transitory and persistent disturbances to scientific measurements, by penetrating via the main and the side lobe of the antenna pattern. However, because of low transmission powers and the source distance of the space generated emissions, they are unlikely to contaminate useful signal in the IF channel.

2.4.2.2 Internal Radio Interference

Radio telescope facilities generate considerable amounts of RFI and many of these electronic equipment that cause interference are mandatory for the scientific measurements. Hence, their installation and operation can never be prohibited. In spite of this, there are approaches that engineers can utilize during the design stages of the observatories to minimise their influence on the measured data. Essentially, the emissions from these devices ought to be detected and prevented from reaching the receiving antenna and its receiver. This can be done by either shielding the radiating device or completely isolating it from the observatory. Regrettably, this is never practised at all times because of realistic and financial reasons.

Table 2.2 gives some internal radiating electronic devices. Their influence on radio astronomical measurements depend considerably on the architectural design of the telescope facility and how well it is shielded. All these separate emitting equipment jointly, nonetheless, can cause background interference at the telescope site. This can continuously contaminate the astronomical data.

Table 2.2: Internal RFI sources installed inside some radio telescopes [27, 28, 29].

RFI from Scientific Instruments	Infrastructural RFI/ Others
Hydrogen Maser	Computers, laptops, screens
Servo amplifiers and power supply	Wireless applications; bluetooth; WLAN
Elevation jack screw motor	Fluorescent lamp
Receiver indexer (RI) encoder	Heating, ventilation, air conditioning (HVAC)
Signal generator, spectrometers	Microwave oven
Indexer motor	Cell phones

Instruments such as hydrogen maser is mandatory for the operations of the telescope but it is a wideband radiator between 1–7 GHz [27]. It should be enclosed in a special chamber known as Faraday cage. Bluetooth wireless services should be banned, because they use 2.4 GHz for data transfer with fairly high power levels ranging between 1–100 mW [28]. Another obligatory piece of equipment is the telescope steering servo electronic that is used to navigate the telescope. However, it also generates wideband interference, hence it requires proper shielding [27]. Also, poor quality LED and fluorescent lamps should be avoided due to their wideband emissions. There are also several built–in micro–radiating components operating as antennas from hundreds of MHz to a few GHz in computing devices such as personal computers and notebooks. In addition, cables that are used to connect personal computers to external storage devices can radiate significant amounts of interference and ought to be considered suspects. Relatively high interference sources are the computer monitors (TFT and CRT), possibly due to poor internal shielding. Generally,

most of the essential high speed digital measuring instruments that leak wideband radiation are contained inside a radio observatory. Even the RFI mitigation tools that are utilised in excising undesired signals from the baseband of the receivers can produce abundant levels of radiation. Narrow band RFI can be generated when a poor quality RFI monitoring system radiates the energy back through the antenna connection [28].

2.4.3 Detrimental RFI Levels

The existence of RFI, either internal or external, will disrupt scientific observations in several ways. In the extreme cases, high RFI levels can lead to saturation of the receiver's amplifier response or malfunction. For instance, when the power level of the noisy signal is between ∼0.1 and 0.01 W, some GaAs–FET and HEMT amplifiers would be damaged. The radiation that leaks in through the isotropic side lobe would give a corresponding power flux density of -10 to +40 dBW/m^2 [30]. And based on the installed receiver and the amplifier, the value which will impose 1 % gain compression in the amplifier's response is approximately in the range of -70 and -30 dBW/m^2 at centimetre wavelength, when the RFI enters through the isotropic side lobe [30]. The sensitivity of the receiver as depicted by equation (2.11) in section 2.3, is determined by the system noise temperature, T_{sys}. The tolerance towards the RFI should be compared to the sensitivity of the receiver (equation (2.15)). Usually, a 10 % tolerance of the RFI power level with reference to the system noise is considered sufficient for normal astronomical observations.

$$\frac{N_{RFI}}{N_{SYS}} = \frac{F_{RFI}\frac{\lambda^2}{4\pi}}{kT_{sys}B} \tag{2.15}$$

where F_{RFI} is the flux density of the RFI. The detrimental levels of interference, F_{RFI}, in single–dish total power radio telescope is equal to a tenth of the r.m.s noise level which gives the threshold for the data, see equation (2.16) below [30].

$$F_{RFI} = \frac{0.4\pi f^2 kT_{sys}\sqrt{B}}{c^2 G_a \sqrt{\tau}} \tag{2.16}$$

where k is the Boltzmann constant, B is the observed bandwidth, G_a is the antenna gain, c is the speed of light and τ is the integration time utilised in the survey. The equivalent equation for the RFI threshold in Very Long Baseline Aperture–synthesis (VLBA) is given by:

$$F_{RFI} = \frac{0.4\pi f^2 k T_{sys} B}{c^2 G_a} \tag{2.17}$$

In the VLBA survey, where measurements are based on correlation, the noise level that would cause damage is 40 dB greater than in a single–telescope survey. The detrimental threshold level of RFI for the continuum and the spectral line surveys are given in [8], see Table 2.3.

Table 2.3: Threshold levels of harmful interference in the continuum (left) and the spectral line (right) observation. In these approximations, the antenna gain is 0 dBi and the integration time is 2000 s.

Continuum observation freq.[MHz]	Channel bandwidth Δf[kHz]	Noise temp. T_{sys}[K]	Interference levels S[dB(W/(m^2 .Hz))]	Spectral observation f_C[MHz]	Channel bandwidth Δf[kHz]	Noise temp. T_{sys}[K]	Interference levels S[dB(W/(m^2 .Hz))]
325.3	6.6	100	-258	327	10	100	-244
1413.5	27	22	-255	1420	20	22	-239
2695	10	22	-247	1612	20	22	-238
4995	10	22	-241	1665	20	22	-237
10650	100	22	-240	4830	50	22	-230
15375	50	30	-233	14488	150	30	-221
22355	290	65	-231	22200	250	65	-216
43000	1000	90	-227	43000	500	90	-210
89000	8000	42	-228	88600	1000	42	-208

2.4.4 Characterization and Detection of RFI

It is a major requirement in radio astronomy to identify, characterize, and mitigate RFI signals. Every RFI signal has a number of unique characteristics, which can be utilized to characterize the signal. Some of the characteristics are: strength, geographical location or position of the source, polarization, directivity, orientation, periodicity over time, bandwidth, frequency distributions, modulation and coding schemes [31]. Characteristics, such as signal strength, are easy to detect for a single source, while others, such as polarization, are more difficult to determine.

Characterizing a particular signal is useful, as it becomes much easier to locate the source and either design it out or have it switched off. Or if that is not possible, the signal can be dealt with during the processing of the data collected, through RFI detection algorithms. Also, being aware of the polarization of the signal is valuable, because astronomical signals are very weakly polarized if at all, whereas RFI is normally strongly polarized.

Characterization impacts on the detection algorithms in that two signals can be compared if they have been characterized, and so it is possible to determine RFI signals through similarity with known RFI. It is important to know the radio atmosphere around the sensitive equipment and to be alert when something changes, to make predicting behaviour easier [31].

The objective of RFI detection and characterization especially in computational algorithms, is to identify the signals for ease of management, flag the signals, and then mitigate the RFI in a manner that will lose the least possible astronomical data. This can be done by removing a point (frequency, time) which has been flagged [2].

2.5 RFI Monitoring Techniques and Equipment

In order to manage the nearby RF environment at the site of the telescopes, different RFI monitoring tools are employed in scanning that environment. The number of radio applications is constantly increasing and this leads to deterioration of the RF spectrum annually. Therefore, persistent RFI monitoring is imperative. Basically, the equipment used to do such on–site measurements consist of an antenna, an amplifier, a receiver such as spectrum analyser and a signal generator. The nearby radio environment is usually scanned with the antenna fixed at either vertical or horizontal polarization from various directions. The choice of RFI monitoring frequency band depends on the frequency band that scientists utilise during the surveys. The section of the frequency spectrum where the IF channel of the radio receiver is assigned, must be scrutinized too. These down–converted IF signals are typically assigned in the range of 300–3000 MHz.

During the RFI field measurements, the antenna should be positioned at the same height as the actual radio telescope. There are two ways in which directional information on the RFI can be collected. The first one is to mount the antenna on a revolving mast, which is set to stop, say, in six orientations as it sweeps through the desired frequency spectrum. The other alternative is to fix, say, six antennas on a mast every 60^o and then set them to sweep the horizon separately. Generally, Log–periodic dipole antennas (LPDAs), with antenna gain of 4 to 7 dBi are effective low cost choice for this type of measurements. The sensitivity S ($\mathrm{Wm^{-2}\ Hz^{-1}}$) of the receiver system is a critical variable, calculated by using the following equation:

$$S = \rho(\varepsilon D)^{-1}.4\pi f_c^2 C^{-2}.kT_{sys}.(\Delta f \tau)^{-0.5} \tag{2.18}$$

where ρ is the polarization mismatch, ε is the efficiency of the antenna, D is the directivity of the antenna, T_{sys} is the system temperature of the receiver system, Δf is the channel bandwidth and τ is the integration time. A low–noise–amplifier can be used to enhance the sensitivity of the receiver system. The sensitivity of RFI–monitoring system is said to be ideal if it matches the far–side–lobe sensitivity of a low noise radio telescope [32]. The utilised channel bandwidth in RFI–scanning system commonly ranges between 10–500 kHz. On balance, the sensitivity of a receiver system should be adequately good to identify the detrimental emission levels given by [8].

To gather the RFI data, a laptop is connected to the receiver (spectrum analyser) through a network cable. The harvested data is then stored and analysed using software such as MATLAB.

2.6 Layers of RFI Mitigation

Mitigation means any method aimed at avoiding RFI signals in the data (category I); removing the RFI from the data (category II); or reducing / eliminating the impact of RFI on the data (category III). This section discusses the promising pro– and reactive mitigation strategies used during celestial surveys.

- **Category I**: This deals with the pro–active measures to change the RFI environment, coordination and management. It is implemented during the design stages of the infrastructure. However, the implementation can also be an operational procedure during the operations stage. In this approach, data is never corrupted. *Prevention is better than cure.*
- **Category II**: The corrupted data is not discarded. Excision is used to identify, flag, and remove corrupted data.
- **Category III**: Reduction of RFI impact on corrupted data through scientific algorithms such as spatial nulling or adaptive spatial filtering, waveform subtraction anti–coincidence is done.

2.6.1 Pro–active Mitigation Strategies

Like other radio telescopes, the MeerKAT and SKA is not immune to the negative effects of some RFI. One of the best ways of minimizing RFI around a radio telescope is to establish a radio quiet region. This involves putting legislation in place that prohibits transmitting

or receiving radio devices within a certain distance of the telescope. However, growth of nearby cities cannot be curbed (as discovered at the Medicina telescope in Italy [33]) and often the radio quiet region is encroached upon. In essence, the site identification should be such that the interference received by the radio astronomy station concerned does not exceed the threshold necessary for this station to operate at its maximum sensitivity i.e where a radio–quiet environment exists. As an example, modelling indicates that terrain suppresses interference by ∼100 dB for both the Hat Creek Radio Observatory and the Green Bank Telescope. This is in addition to the normal propagation loss [34, 22]. The theoretical propagation studies and digital terrain models conducted by the South African SKA team confirmed the shielding effect of terrain on RFI [22]. From the above, and given the sensitivities that are to be achieved, it then follows that the choice of a radio–quiet site is paramount [35].

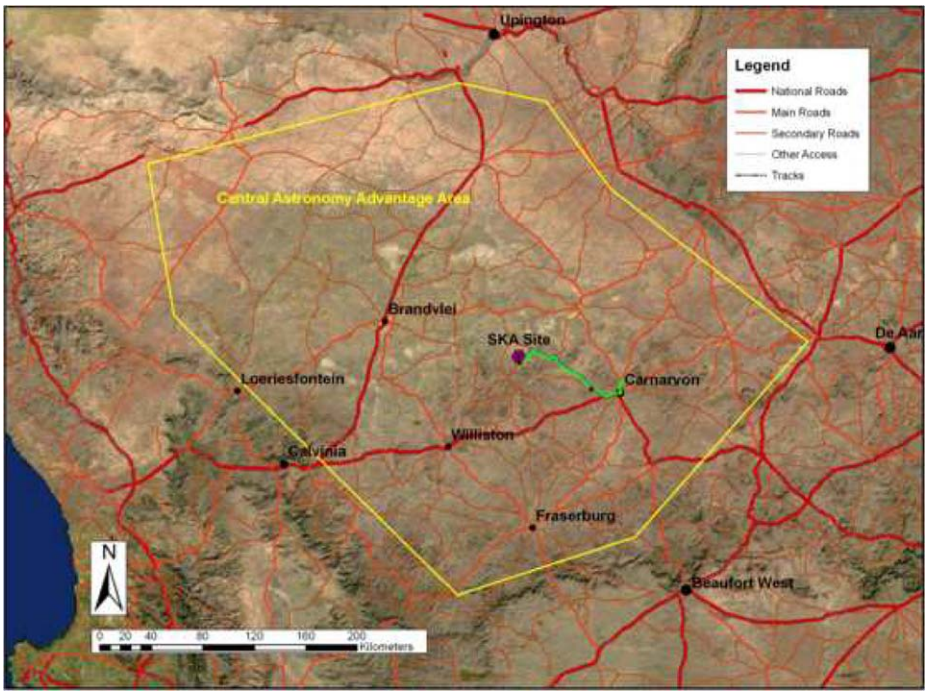

Figure 2.7: Map of the area and expanse of the remote region in the Northern Cape province of South Africa. The central region with a purple dot and marked "SKA Site" is the setting for the inner core(s) of the SKA and the MeerKAT. The estimated distance (90 km) between the site and the nearest small town (Carnarvon) is traced by the geen line[7].

Following the above reasons, the MeerKAT and SKA projects are based in the Karoo, far from any large settlements. The Astronomical Advantage Act enforces restrictions on frequencies by region (shown in Figure 2.7). These regions surround the core of the MeerKAT and SKA projects. Unfortunately, it is not possible to find a region which is absolutely radio quiet, no matter what regulations are put in place. South Africa's trump card is due to its geographical advantage and the suitability of its site on the

basis of lowered RFI emissions. Transmitters are operating at lower power and mobile communication tower designed antennas which have nulls in core site direction. In addition, satellites and aeroplanes still pass overhead. Beyond radio quiet regions, the International Telecommunications Union (ITU) have released a table specifying frequency allocations for different types of communications. This table is managed by the communications authority of each country.

The Independent Communications Authority of South Africa (ICASA) has released the relevant table for South Africa [36]. This allocates a relatively small number of narrow frequency bands to radio astronomy, and normally these bands are shared with other communication areas. It is illegal for a signal to be transmitted outside the allocated frequency, and so signals detected in these area can be turned off by the authorities (ICASA). If radio astronomy wishes to make use of other frequency bands, there will be a large amount of RFI which is entirely legal.

As mentioned earlier in subsection 2.4.2, the observatories themselves can contribute to significant levels of self–generated RFI. However, such emissions can be minimised through careful design procedures such as screening the equipment that radiate electromagnetic energy inside a Faraday cage and ban the operation of radio broadcasts [28]. Also, radio receiver design plays a crucial role on the quality of the measured scientific data. Receivers are commonly planted within screened metallic boxes, which lessen the RFI substantially. Similarly, in the receiver, some analogue electronics are placed within shielded boxes to reduce their emissions on the other units [37].

2.6.2 Reactive Mitigation Methods

It is worth noting that some of the existing telescopes are content with their ambient radio environment and the effectiveness of the pro–active mitigation strategies. However, depending on the nature of the scientific study to be done and the surrounding environment, the application of reactive mitigation techniques (categories II&III) might be obligatory. This subsection discusses some of the promising algorithms in radio astronomy.

2.6.2.1 Spatial Filtering

The aim of spatial filtering is to minimise the RFI levels in a sample to the point where they can be “seen through” to view the astronomical signals. The technique is applied in multichannel radio astronomical survey to eliminate persistently present RFI like the television signals, radio broadcast and the GPS satellite systems [38]. It is based on the

difference between the direction–of–arrival (DOA) of the interferer and the direction of the signal–of–interest (SOI). Also, it can be used in a single dish observation, where a low gain auxiliary antenna is used to detect the interferer. Spatially confined RFI within the vicinity of the telescopes, can be contained to lowest levels by directing the zeros of the synthesized antenna pattern towards the DOA interference. This kind of null–forming is a comparatively efficient technique against RFI from the telecommunication satellites, such as GPS and GLONASS. Nonetheless, it is deemed less efficient against ground–based interferers, due to the scattering effects and the multipath propagation of the interfering signals.

2.6.2.2 Spectral Kurtosis

Real–time identification and removal of the RFI from scientific data with Spectral Kurtosis (SK), has been demonstrated to be so efficient that it may become a benchmark for the next generation radio sensors. It is a statistical method that naturally works on time averaged, non–Gaussian data, though it can be extended to work on other types as well. SK is a thresholding method, applied either during or after the fast Fourier transform (FFT), and is applied equally well in frequency and time domains. The SK can be calculated using:

$$V_k^2 = \frac{\sigma_k^2}{\mu_k^2} \tag{2.19}$$

where σ_k^2 is the variance and μ_k^2 is the mean of the power spectral density (PSD). A sample with no RFI will have $V_k^2 = 1$. Calculating the mean and the variance is done for M spectral estimates, P_{ki} where k is the channel number, and i = 1,....,M. These are used to calculate the instantaneous PSD, S_1 and the squared spectral power S_2,

$$S_1 = \sum_{i=1}^{M} P_{ki} \tag{2.20}$$

$$S_2 = \sum_{i=1}^{M} P_{ki}^2 \tag{2.21}$$

Then the mean and variance are given by:

$$\mu_k = \frac{S_1}{M} \tag{2.22}$$

$$\text{and} \quad \sigma_k^2 = \frac{MS_2 - S_1^2}{M(M-1)} \tag{2.23}$$

$$\text{This gives} \quad V_k^2 = \frac{M}{M-1}\left(\frac{MS_2}{S_1^2} - 1\right) \tag{2.24}$$

The variance of V_k^2 is then calculated, and compared to the expected value of:

$$var(V_k^2) = \begin{cases} \frac{24}{M}, & k = 0, N \\ \frac{4}{M}, & k = 1, ..., (N-1)[39] \end{cases} \tag{2.25}$$

where N is the Nyquist rate associated with the sampling rate. The Nyquist rate is the lowest rate at which a signal can be sampled without introducing errors; it is twice the highest frequency of the signal. If the variance is significantly different, the signal can be considered to be RFI.

A good implementation of the SK method requires a full understanding of all the statistical techniques involved. The complexity of the algorithm will depend on how many windows of size M are used. The SK method is suitable for use on any type of data, but as a purely statistical method, it does not hold much interest from a computing perspective.

2.6.2.3 Time and Frequency Blanking

Temporal blanking is perhaps the oldest and best–known technique for real–time mitigation of pulsed RFI, which is used as a response to ground–based aviation radars operating in the 1215–1400 MHz band [40]. The Main idea is that an observer sets a threshold level, that is used to distinguish RFI from the RFI–uncontaminated data. If the threshold level is exceeded by the presence of RFI, the corrupted portion of the signal will be excised, see Figure 2.8.

The blanking operation can be done on analogue, pre–processed data as well as on digitalized samples. It has the following advantages:

- Simple to understand
- Easy to implement
- Fast (has low complexity)
- Simple to automate and

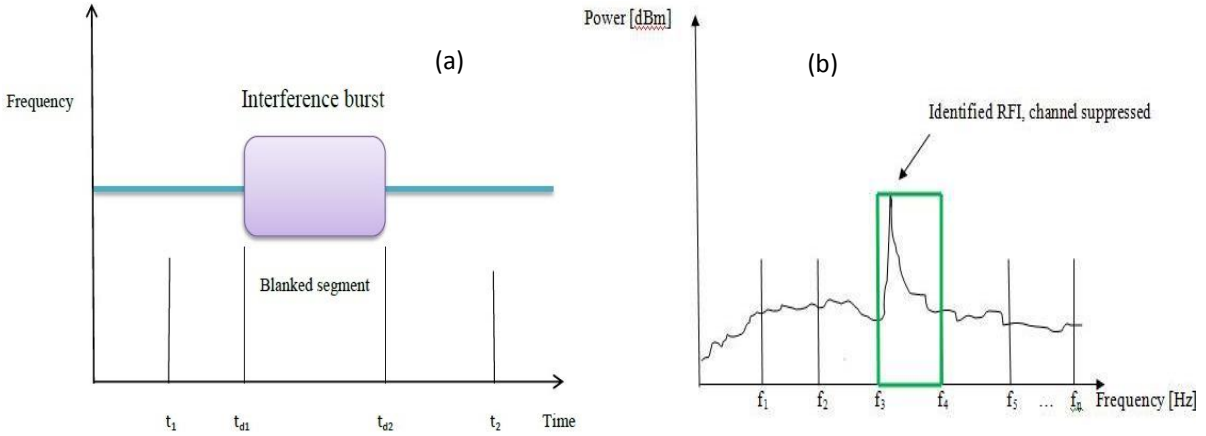

Figure 2.8: Illustration of time and frequency blanking where (a) shows time blanking: The segment that exceeds the threshold level is removed and (b) frequency blanking: The corrupted frequency channel is suppressed [41].

- Effective

As astronomy pipelines already are computer intensive, low complexity is the most important fact that makes scientist choose this strategy.

However, it has its own downside: The approach fails to protect the desired signal against persistent broadband RFI. The only technical requirement in this method is the tapped observation bandwidth that would require the processor to run on a digitised data stream several hundreds of megasamples/second [42]. Regrettably, weak and constant radio interferers cannot be detected in the time domain by using a threshold.

With the fact that modern software telescopes are real–time systems, sometimes it is impossible to implement sophisticated blanking in time strategies. Instead, it is a better strategy to iterate the data in frequency order, while identifying frequencies that have RFI. In frequency blanking, the observation band is split into several equal sized channels, Δf, where the RFI corrupted channel is just extinguished, as in Figure 2.8 (b).

2.6.2.4 Interference Cancellation Using Auxiliary Antenna

Interference cancellation strategies involve adaptive and post–correlation processes, which are normally dominant over excision techniques for removal of low level RFI. For instance, excision method like simple blanking results in data loss. However, the principles of operation are primarily similar in both techniques; the produced artefacts are extinguished to lowest levels by the use of a reference data–channel. The weak radiometric signal, X_S, in the main lobe is usually contaminated by the existence of a much stronger interference signal, RFI_{main}, that has leaked through the side lobe (Figure 2.9). A low gain auxiliary

antenna which connects to another receiver is directed towards the interferer, RFI_{ref}. The reference signal is then input to the adaptive filter for optimizing the filter coefficients to mitigate the RFI signal. Both interference signals from the two receivers are correlated and then through the adaptive filter a real–time estimation of the correlation is done.

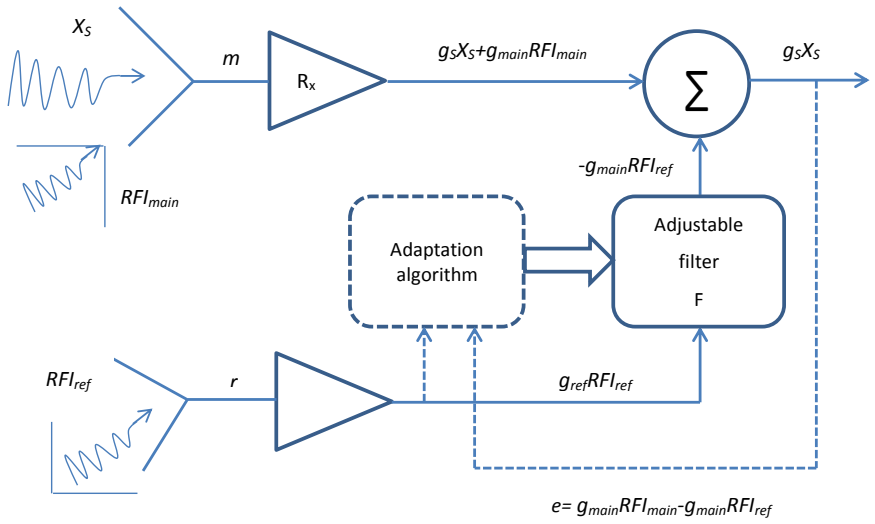

Figure 2.9: A demonstration of adaptive cancellation method in mitigating the interference signal.

Through the adaptive algorithm the previous and the present samples are compared and then an update is sent to the digital filter. That is to say, it aims to cancel out the effect of the various propagation paths, so that the error signal, $e = g_{main}RFI_{main} - g_{main}RFI_{ref}$ $\rightarrow$0, and only the useful signal, g_SX_S, remains [41]. A cancellation technique implemented before correlation can potentially retrieve most of the data from a contaminated sample.

2.6.3 Adoption of Reactive Mitigation Methods

Despite much research on RFI mitigation for the past decade or so, methods other than filtering and simple excision of RFI–contaminated data are not at present widely used in radio astronomy. This is primarily because more complex forms of mitigation require costly hardware, challenging software development and expert–user capability to exploit during or after an observation. In addition radio astronomers are reluctant to move from the *tried and true* to adopt black box methods of mitigation. Some proposed methods are not suitable for real–time operation, but require access to large data sets of recorded signals in a post–acquisition processing mode. Though many mitigation techniques have been tested, it is not possible for any of them to address every issue posed by the diverse variety of

RFI sources. Radio astronomy observations are made with many different objectives that require a variety of different techniques and equipment.

The flow chart below gives a summary of the basic classification of RFI mitigation techniques in radio astronomy. Some of the methods have already been discussed in sections 2.4 and 2.6.

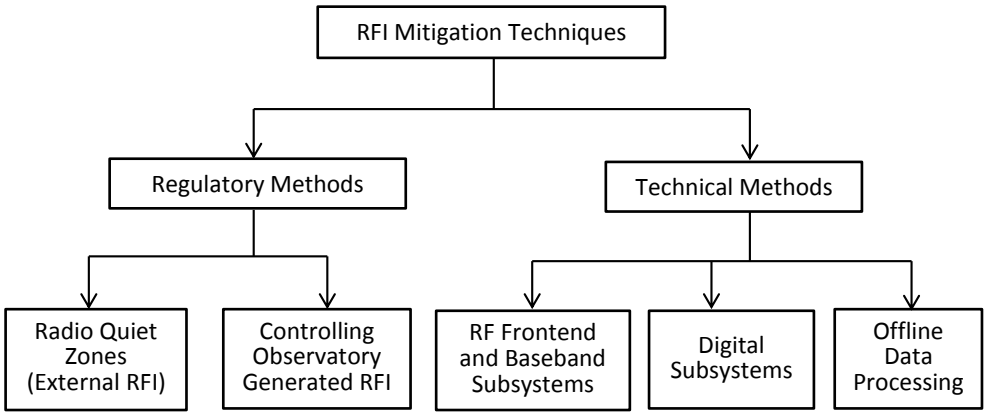

Figure 2.10: Basic classification of RFI mitigation techniques used in radio astronomy.

2.7 RFI Characterization Techniques in Different Environments

The measurement of radiated and conducted emissions can be done in different environments depending on the availability of the facility and the nature of the experiment. Some of the facilities include reverberation chamber, anechoic chamber, open area test site (OATS), FEKO simulation tool and computer simulation technology microwave studio (CST MWS). It is always important to use more than one of these resources for better comparison and accuracy of data.

Computational modelling in FEKO and physical scale measurement in an anechoic chamber were used successfully for RFI characterization of KAT–7 structure [43]. The recommendations from the research resulted into retrofitting of the lightning down conductor (LDC) on the KAT–7 telescope and full implementation of LDC on the MeerKAT dish. In addition, detailed on–site tests for common mode (CM) currents on the KAT–7 telescope using direct injection method at the antenna feed and induced current distribution technique through a plane wave are found in [44]. Together with CST MWS and scale modelling, earth connection studies on the KAT–7 structure were made [44]. Other RF studies that were carried out include: high frequency cable tray measurements in OATS at the Houwteq

facility in the Western Cape Province [44] and EM characterization of the MeerKAT design with specific focus on lightning–induced RFI, lightning surge protection, and earthing [45].

2.7.1 Anechoic Chamber

Electromagnetic compatibility (EMC) tests are normally done on OATS. However, OATS based in low RFI environment and varied weather conditions may lead to inaccurate measurements or damage to electronic equipment. In view of this, EMC measurements are performed in a well shielded room (anechoic chamber) whose internal walls incorporate absorbing materials. The absorbers either scatter or absorb the incident electromagnetic signal so that it simulates the characteristics of "free space". The chamber can be fully anechoic if all the walls are covered by the absorbers or semi–anechoic if the floor is left uncovered [46]. Generally, the structure for the chamber requires less space and measurement schedules are not limited by poor weather conditions. Therefore, it becomes a viable and alternative option to OATS for electromagnetic research experiments.

Most of the anechoic chambers are rectangular in shape because it is simple to put up the structure and much easier to arrange and line the chamber's surfaces with wave–absorbing material. However, the disadvantage of this basic design is the huge scattering caused by the absorbers when the signal approaches at large angles of incidence with reference to the normal direction of the absorbers. Such wide–angle reflections are critical during low frequency measurements, where the absorption power of the chamber is less effective [46]. Consequently, the reflected signal will mix up with the direct–path signal at the test region and create an interference field (with sharp peaks and nulls) which results into errors in the various wave–propagation measurements. Hence, the reason the chamber should be used at intended frequencies.

The chamber at the engineering department, Stellenbosch University, is fully anechoic with a "catwalk" as shown in Figure 2.11. The lining of the chamber's surfaces with pyramidal absorbers has been done precisely, to minimize the discontinuities between the adjacent absorber blocks. The gaps and misalignment of the pyramid absorber blocks may lead to a much poorer reflectivity than the manufacturer's specification. Although the chamber was deigned to operate optimally at frequencies between 2 to 18 GHz, it can work effectively even from 500 MHz.

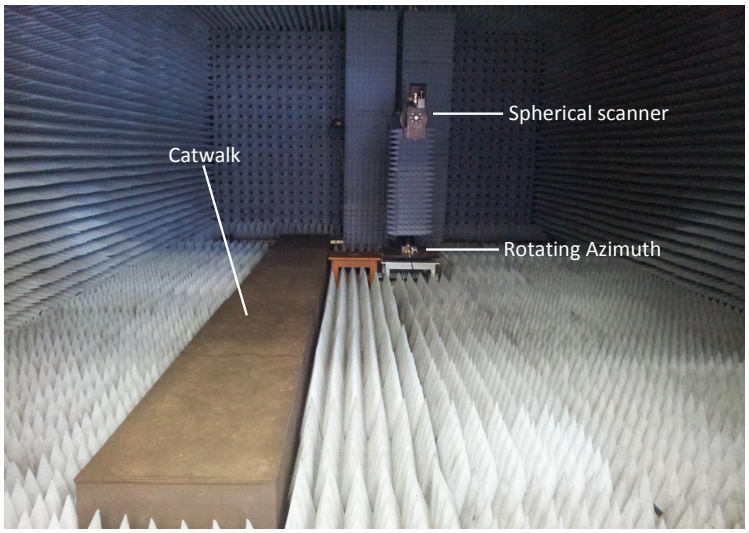

Figure 2.11: Anechoic chamber at Stellenbosch University.

2.7.2 Antenna Calibration Methods

Generally, the accuracy of experimental data depends upon the characteristics of the anechoic chamber, test equipment, cable connections and the antenna used. For the consistency of results, antenna calibration is mandatory. There are two generally used antenna calibration methods namely:

a) The two–antenna (or reference antenna) method and

b) The three–antenna method [47].

For the two–antenna method, the reference antenna has known dimensions and known antenna factor (AF). At each calibration frequency, a field is determined first by the reference antenna and then by the substituted (uncalibrated antenna) or antenna under test (AUT). The AF of the AUT can be determined by getting the difference between the two readings then applied to the actual AF of the reference antenna. The three–antenna method of calibration requires three sets of data collected under similar geometrics using three uncalibrated antennas. The antennas are used as transmit / receive (T_x/R_x) pair combinations e.g (1/2), (1/3) and (2/3). The three unknown antenna factors are calculated based on these three sets [47].

2.8 Summary

The information from the survey was the bedrock upon which investigations on RFI characterization of the MeerKAT structure using computational modelling was initiated.

Validation of the MeerKAT model is an essential process which forms part of this study. Consequently, the verified model can be used with confidence for relevant RFI coupling investigations on the MeerKAT structure.

—Advances are made by answering questions. Discoveries are made by questioning answers —

—Bernhard Haisch —

CHAPTER 3

Methodology and MeerKAT Scale Models

THERE was limited window of opportunity for on–site measurements hence the option for computational modelling. Also, access to physical scale model made it possible for verification of the FEKO models. This chapter explains the basics of computational modelling in FEKO, utilizing the method of moments (MoM). Initial MeerKAT scale model discussed in [45], was characterized in anechoic chamber and verified with an exact computational model. The objective was to ensure that all parts and connections of the simplified model were still in proper condition for consistency of results. A modified MeerKAT scale model which has been retrofitted with a receiver indexer and earth stub–up sections is introduced and replicated in FEKO. In order to trust our computational modelling, the MoM code is verified again with the modified scale model.

The full scale verification of fields with limited field measurements is discussed in chapter 4. The use of validated models for multiple MeerKAT structures in FEKO by duplicating the verified structures, dish to dish coupling can be studied.

3.1 FEKO and Method of Moments (MoM)

The CEM code FEKO is a package of various numerical full–wave and asymptotic high frequency solvers with powerful hybrid combinations as shown in Figure 3.1. The full

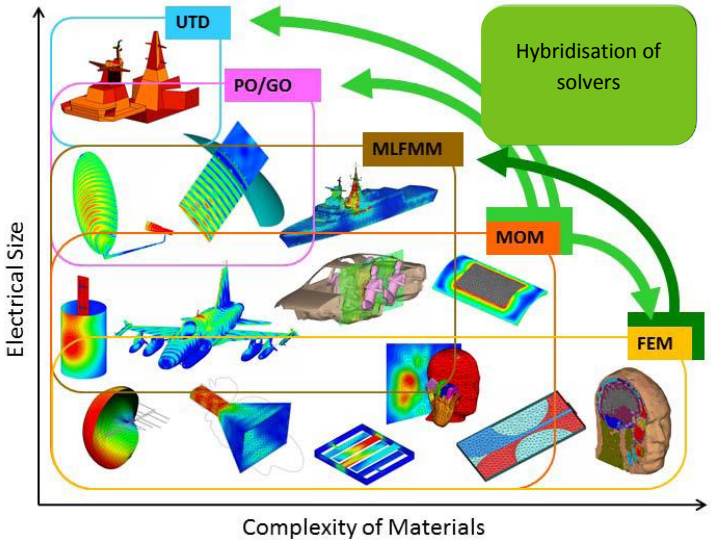

Figure 3.1: Illustration of different solvers available in FEKO [48].

wave solvers that are commonly used in the industry include: the popular MoM (which has been traditionally used in the frequency domain), the Finite Element Method (FEM, frequency or time domain) and the Finite Difference Time Domain (FDTD, time domain) or Finite Integration Method (FIT, time domain) [48]. These techniques are potentially very accurate and the central idea is to discretise some unknown electromagnetic property, typically the surface current for the MoM, and the E–field for the FEM and FDTD methods [49]. This procedure of discretisation is also referred to as *meshing*. It involves subdividing the geometry into a (large) number of small segments. The asymptotic methods such as the Uniform Theory of Diffraction (UTD), Physical Optics (PO) and Geometrical Optics (GO) are generally limited to specific applications.

The Basic Concept of MoM

The MoM can be applied on a problem whose formulation can be expressed as a linear operational equation in the form [49]:

$$\mathcal{L}(f) = g \tag{3.1}$$

where $\mathcal{L}$ is a linear operator which maps function f to g. It can be a differential, an integral or an integro–differential operator. The function f is unknown, say, charge density ρ, and g is a known function, say, voltage on a conductor. In the initial stage of MoM, f is defined over the domain $\mathcal{L}$, $D_{\mathcal{L}}$, as a linear combination of expansion functions.

$$f = \sum_{i=1}^{N} \alpha_i f_i \tag{3.2}$$

where α_i is the i^{th} unknown scalar and f_i is the i^{th} known expansion function usually called the *basis function* in MoM formulation. For an estimate solution, equation (3.2) is a finite summation while for an exact solution, it becomes infinite. The appropriate substitutions between equations (3.1) and (3.2) yields:

$$\sum_{i=1}^{N} \alpha_i \mathcal{L}(f_i) = g \tag{3.3}$$

The next step is to define a set of linearly independent testing or weighting functions, $\{w_1, w_2, ..., w_N\}$, in the domain of $\mathcal{L}$. By multiplying the inner product of equation (3.3) with each value of w_j (integrated over the entire domain) and applying the linearity of the inner product gives.

$$\sum_{i=1}^{N} \alpha_i \langle w_j, \mathcal{L}(f_i) \rangle = \langle w_j, g \rangle \qquad j = (1, 2, 3, ..., N) \tag{3.4}$$

The above equation can be rewritten as follows:

$$\begin{pmatrix} \langle w_1, \mathcal{L}(f_1) \rangle & \langle w_1, \mathcal{L}(f_2) \rangle & \cdots & \langle w_1, \mathcal{L}(f_N) \rangle \\ \langle w_2, \mathcal{L}(f_1) \rangle & \langle w_2, \mathcal{L}(f_2) \rangle & \cdots & \langle w_2, \mathcal{L}(f_N) \rangle \\ \vdots & \vdots & \ddots & \vdots \\ \langle w_N, \mathcal{L}(f_1) \rangle & \langle w_N, \mathcal{L}(f_2) \rangle & \cdots & \langle w_N, \mathcal{L}(f_N) \rangle \end{pmatrix} \begin{pmatrix} \alpha_1 \\ \alpha_2 \\ \vdots \\ \alpha_N \end{pmatrix} = \begin{pmatrix} \langle w_1, g \rangle \\ \langle w_2, g \rangle \\ \vdots \\ \langle w_N, g \rangle \end{pmatrix} \tag{3.5}$$

A simplified matrix form of equation (3.5) is given by:

$$[V] = \{Z\}\{I\} \tag{3.6}$$

$$\begin{aligned} Z_{ij} &= \langle w_j, \mathcal{L}(f_i) \rangle \\ I_i &= \alpha_i \\ V_j &= \langle w_j, g \rangle \end{aligned}$$

where Z is the commonly known MoM impedance matrix and I contains the unknown coefficients. The application of iterative or invasive methods on equation (3.6) gives a

solution to the unknown values of I. Another approach is to decompose the dense matrix Z into two or simpler matrices (normally upper and lower triangular matrices) which simplifies the problem. For an eigenvalue problem, the complex impedance operator Z (see equation (3.7)) relates the surface current to the electric field intensity through the eigenvalue equation (3.8).

$$[Z] = R + jX \tag{3.7}$$

$$[X]\{I_n\} = \lambda_n[R]\{I_n\} \tag{3.8}$$

where λ_n is the eigenvalue corresponding to the n^{th} characteristic current, I_n, while R and X are the real and imaginary parts of the MoM impedance matrix, Z, respectively. The characteristic currents determined from the solution of equation (3.8) are real and orthogonal functions and depend only on the shape and size of the conducting body [50].

In summery, the MoM technique replaces the radiating/scattering structure with surface currents which are discretised into smaller segments resulting into a surface mesh [49]. This leads to the formulation of a matrix equation which computes the effect of a particular mesh segment on every other mesh segment through the utilization of the Greens function. The MoM–based CEM code, FEKO, is chosen due to its efficiency on metallic surfaces and open boundaries. Only the surface of a conducting body is meshed; while the so called "air region" surrounding the antenna is unmeshed. The calculation of fields is now possible through the known impedance and segment currents. The MoM code has been used throughout this research for verification purposes and RF studies on the MeerKAT structure.

3.2 Characterization of the Initial MeerKAT Scale Model in an Anechoic Chamber

Two LPDA antennas and a MeerKAT scale model are used for the calculation of the gains through the three–antenna method. The gain of an antenna can be used to determine an antenna factor, AF, which is important for the characterization of an antenna [51]. By using the Friis radio link equation (2.9), in each of the three antenna measurements, three equations can be written as:

$$|S_{21\_l_1-l_2}|^2 = \frac{G_{l_1}G_{l_2}\lambda^2}{(4\pi R)^2} \tag{3.9}$$

$$|S_{21\_l_1-l_{kat}}|^2 = \frac{G_{l_1}G_{l_{kat}}\lambda^2}{(4\pi R)^2} \tag{3.10}$$

$$|S_{21\_l_2-l_{kat}}|^2 = \frac{G_{l_2}G_{l_{kat}}\lambda^2}{(4\pi R)^2} \tag{3.11}$$

where the subscripts l_1, l_2 and l_{kat} refer to the specific LPDA and MeerKAT antennas respectively, S_{21} is the transmission coefficient measured from the vector network analyser (VNA), λ is the corresponding wavelength at each calibration frequency, and R is the distance between antenna phase centres. The value for R was measured as 5 m inside the chamber and the measurements were done from 45 MHz to 3 GHz with 201 frequency points. Using the substitution method on the three equations above, the three unknown gain functions can be solved by the following equations:

$$G_{l_1} = \frac{|S_{21\_l_1-l_2}||S_{21\_l_1-l_{kat}}|(4\pi R)}{|S_{21\_l_2-l_{kat}}|\lambda} \tag{3.12}$$

$$G_{l_2} = \frac{|S_{21\_l_1-l_2}||S_{21\_l_2-l_{kat}}|(4\pi R)}{|S_{21\_l_1-l_{kat}}|\lambda} \tag{3.13}$$

$$G_{l_{kat}} = \frac{|S_{21\_l_1-l_{kat}}||S_{21\_l_2-l_{kat}}|(4\pi R)}{|S_{21\_l_1-l_2}|\lambda} \tag{3.14}$$

The gain functions for the three antennas are given in appendix B. The antenna calibration set up is shown in Figure 3.2 and includes a 40 dB permanently installed amplifier driving into port two of the VNA. The role of the amplifier is to allow more sensitive measurements to be done by improving the system's dynamic range. Also, it counteracts the appreciable losses in the signal strength when longer cables are used inside the chamber. The schematic only shows two LPDAs connected to port one and port two of the VNA but the MeerKAT scale model that was used as a third antenna is shown in Figure 3.9 (a).

Finally, the linear values for $G_{l_{kat}}$ from equation (3.14) are converted into decibel scale ($G_{l_{kat}}(dB) = 10log(G_{l_{kat}})$) before being used in equation (2.6) (refer to subsection 2.1.7 of the previous chapter) to obtain the AF for the MeerKAT scale model. In order to validate the calculated values of AF from measurements, an exact computational, FEKO model of the MeerKAT is illuminated with a plane wave as shown in Figure 3.3.

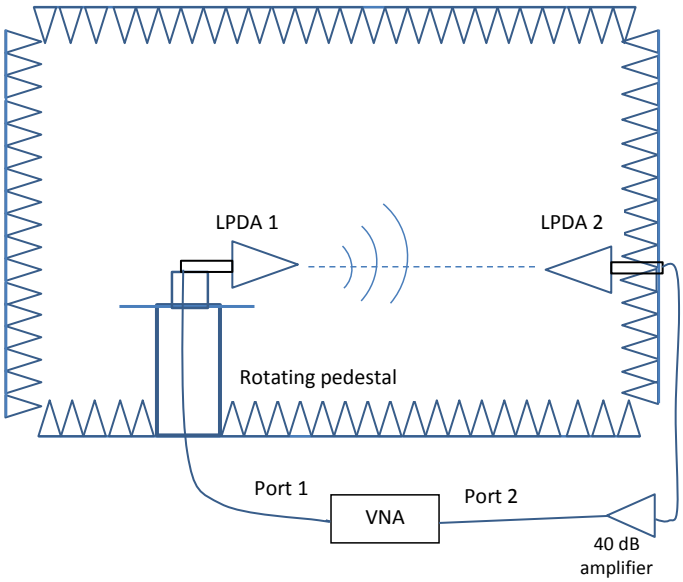

Figure 3.2: Schematic illustration of the set up for the antenna calibration measurements inside anechoic chamber.

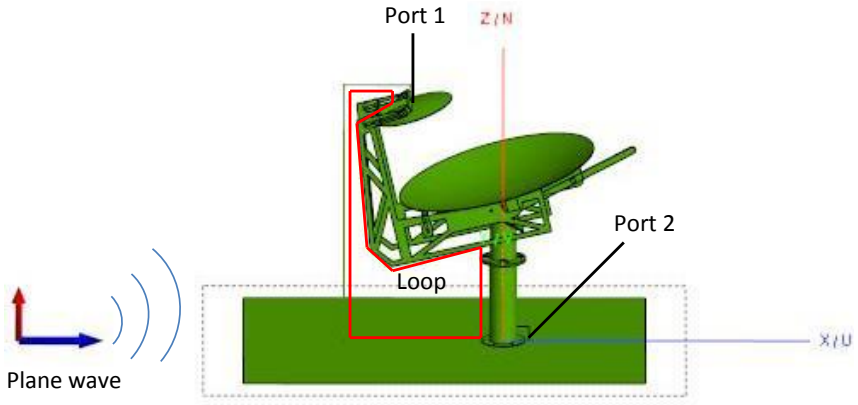

Figure 3.3: FEKO model of MeerKAT (90^0 orientation) being illuminated with electromagnetic (EM) plane wave of magnitude 1 V/m .

The placement of the MeerKAT model, relative to the plane wave as in Figure 3.3 was chosen as a ninety degree (90^0) angle of orientation for optimum coupling of the incident field into the loop. This was the same orientation of the scale model inside the anechoic chamber. The electromagnetic (EM) plane wave with vertical E–field and horizontal H–field orientations was defined with a value of 1 V/m in FEKO [43], which simulates the scenario in the anechoic chamber where the LPDA antenna illuminates the scale model of the dish. The ports were modelled as being 50 ohm and were used to request for the currents in the simulation. After the meshing of the model, 42 segments and 62,459 discrete triangles were obtained. It took approximately two and half hours for a complete single frequency run, in a 256 GB RAM, 12 core university computer (Babbage). There were 100 frequency points used in a 45 MHz–3 GHz range. From the general ohmic relationship

between voltage and current the output linear voltage can be calculated from equation (3.15).

$$V_{out} = 50I \tag{3.15}$$

where I refers to the requested linear currents through the 50 Ω load. The ratio of V_{in} (1 V/m) to V_{out} gives the antenna factor, AF, as [16]:

$$AF = \left(\frac{V_{in}}{V_{out}}\right) \tag{3.16}$$

However, if one has the values for transmission coefficient, $S_{21-FEKO}$, which have been computed from FEKO, then these can be used as well together with equation (3.11) to obtain the gain function for the FEKO model. These values for the gain can in turn be utilized in equation (2.6) to calculate the AF. The comparison between the measurement and the FEKO simulation for AF are shown in Figure 3.4; the results show a close agreement across the frequency band. A similar set up was used with a KAT–7 scale model that was initially built and verified for lightning–induced RFI and earthing investigations [43].

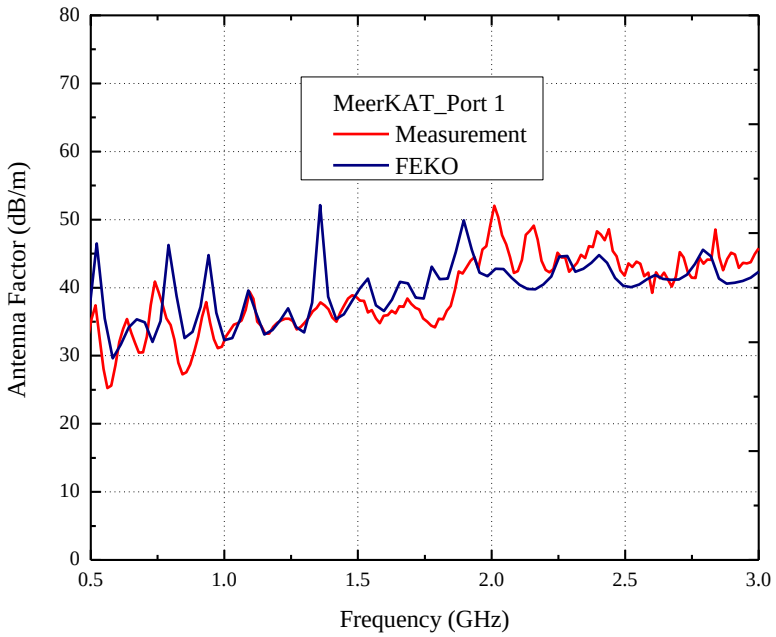

Figure 3.4: Comparison between the measurement and the FEKO simulation for AF.

For a zero degree (0^0) angle of orientation of the MeerKAT model, the plane of the bigger loop that connects to port 1 is parallel to the horizontal H–field of the wave as depicted in Figure 3.5 above. The plots for the gain functions when the mock–up is in the zero

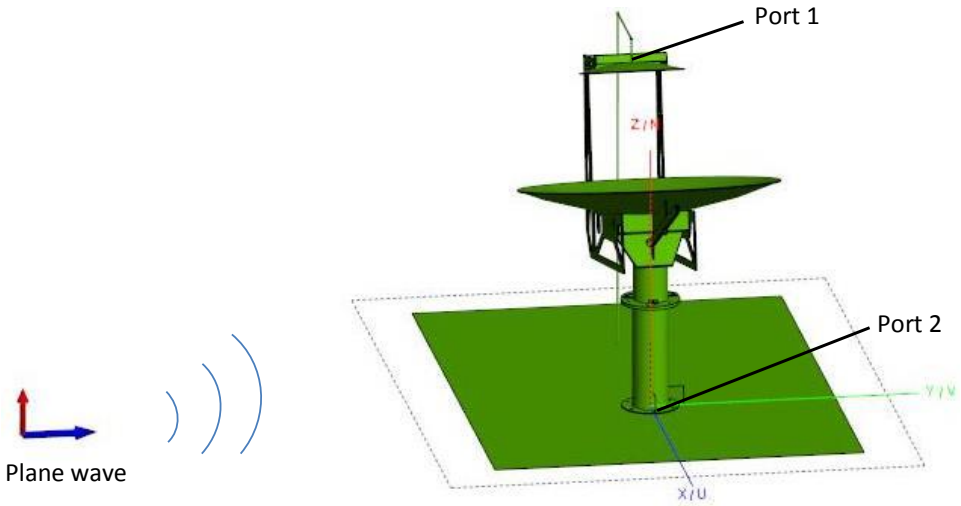

Figure 3.5: MeerKAT FEKO model (0^0 orientation) being illuminated with electromagnetic (EM) plane wave of magnitude 1 V/m.

or ninety degrees direction are given in Figure 3.6. In order to extract some meaningful information from the graphs, an average value for the gains is calculated. The mean value for the gain for 0^0 angle of orientation is -4.1 dB while that for 90^0 is -2.8 dB. This difference in the average gains is as expected since the incident horizontal H–field is perpendicular and parallel to the plane of the loop in the zero and ninety degree angle orientations, respectively. Therefore, the induced field in the loop for the second set up (Figure 3.5) is not as significant as in the first set up.

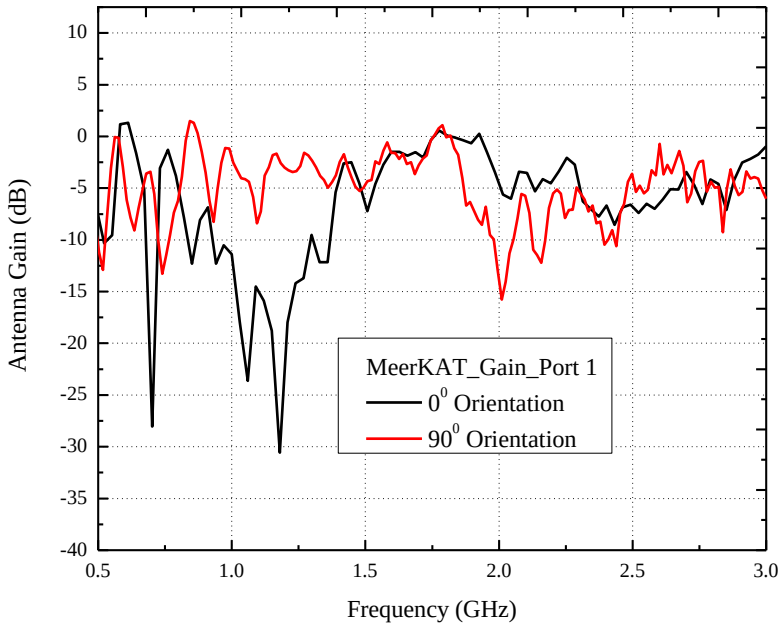

Figure 3.6: Comparison of the gain functions for the MeeKAT model, positioned in two different directions relative to the incoming plane wave.

After a successful validation of the initial model, areas of interest could be added to the model for further verification as detailed in the subsequent section.

3.3 Modified MeerKAT Design $1/20^{th}$ Scale Models

A simplified physical mock–up of the early MeerKAT dish design which was scaled down by a factor of 20 is shown in Figure 3.9 (a) subsection 3.3.3. This scale model together with a CEM model in FEKO were used in EM characterization of a single dish structure [45]. It is the same model which has been characterised in the previous section for the reasons mentioned earlier. With minor additions, it was expanded to include the RI and stub–up representative sections of the actual dish. This required verification of the additions and to confirm repeatability of previous characterisation. These two critical parts of the MeerKAT antenna are briefly discussed.

3.3.1 Receiver Indexer (RI)

The RI of the MeerKAT dish is a metallic bench where shielded electronic components, the UHF and L–Band receivers are mounted. Its top section where the receivers are installed is semicircular in shape and behind the receivers where other electronics are located it is more rectangular. Both the sub–reflector and the RI are configured with the connecting structure such that they are below the main reflector for easy access and servicing (Figure 3.7 (a)). The RI can accommodate a maximum of four receivers and one of its key functions is to allow precise positioning of a particular receiver at the secondary focus of the ellipsoidal sub–reflector [29]. Figure 3.7 (b) is a zoomed photo view of the RI region and the sub–reflector.

Most of the cables from the RI are connected to various electrical components of the telescope. Connectors are mostly used to join these cables to different electronics which serve different purposes on the telescope. In electromagnetic compatibility (EMC), a possible entry point for RFI would include cable shields or connectors as pointed out in chapter 2 subsection 2.4.2. Therefore, it was important (during field measurements) to do investigations on the current levels that could couple into various cables of the MeerKAT sensor using simulated fields.

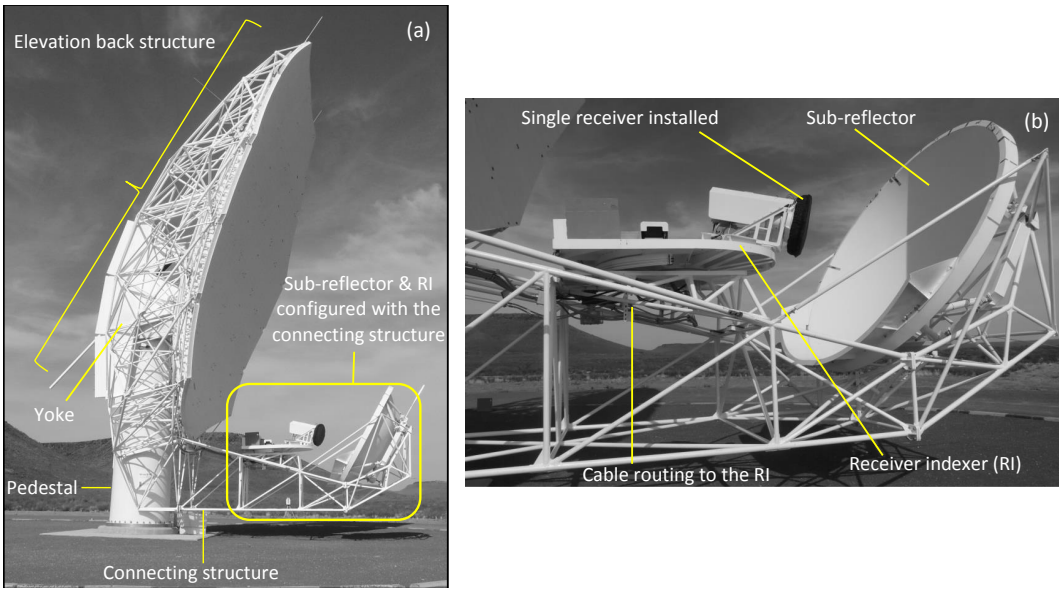

Figure 3.7: (a) 13.5 m Gregorian dual offset MeerKAT antenna (side view) (b) A close up view of the sub–reflector and RI with cable routing to its various components such as vacuum pump box and receivers.

3.3.2 The Stub–Up

It is stated that a greater percentage of EMC problems are caused by inadequate layout and earth termination of cabling systems [52]. For this reason, great care has been taken in designing the MeerKAT structure cable entry point, where a special earth stub–up was used for shielding purposes. The objective is to ensure proper shielding is maintained at the cable entry point by connecting cable shields with 360 degree connections [52]. You can have the best shields in the world, but if you take cables through a hole in the wall, your interference will go through as well due to CM coupling onto the cable.

Figure 3.7 (a) shows the pedestal which is connected to the foundation and supports the yoke as well as the elevation structure. The stub–up is located inside the pedestal. In the stub–up, the mains power and three separate earth connections enter through a steel–wired armoured cable gland. The three earth connections are joined together at the stub–up cap and a single earth cable (the green cable in Figure 3.8 (b)) is then taken further to the main earth bus–bar. Part of the investigation aims to quantify the level of shielding the stub–up provides. The inclusion of the RI and the stub–up in the physical and CEM scale models is described in subsections 3.3.3 and 3.3.4, respectively.

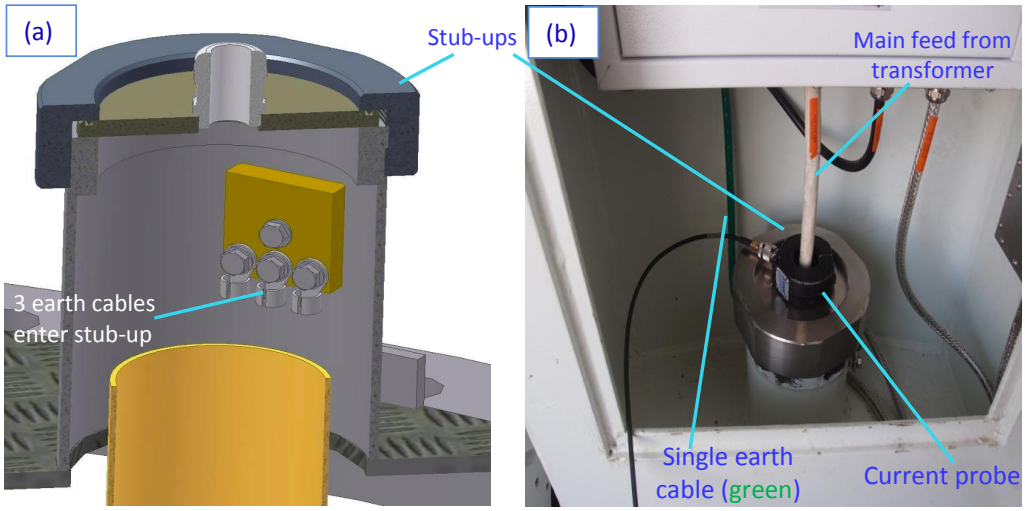

Figure 3.8: (a) Power stub–up design: Internal view [29] (b) A photo of the stub–up inside the actual MeerKAT dish.

3.3.3 Physical Scale Model

Figure 3.9 shows two simplified scale models: One with and the other without the characteristic part of the RI. The entire model is mounted on a 120 mm by 180 mm conducting ground plane. The inset photo in Figure 3.9 (b) is a zoomed front view of the RI section with three receivers and a semi–rigid cable that is connected to the metallic box.

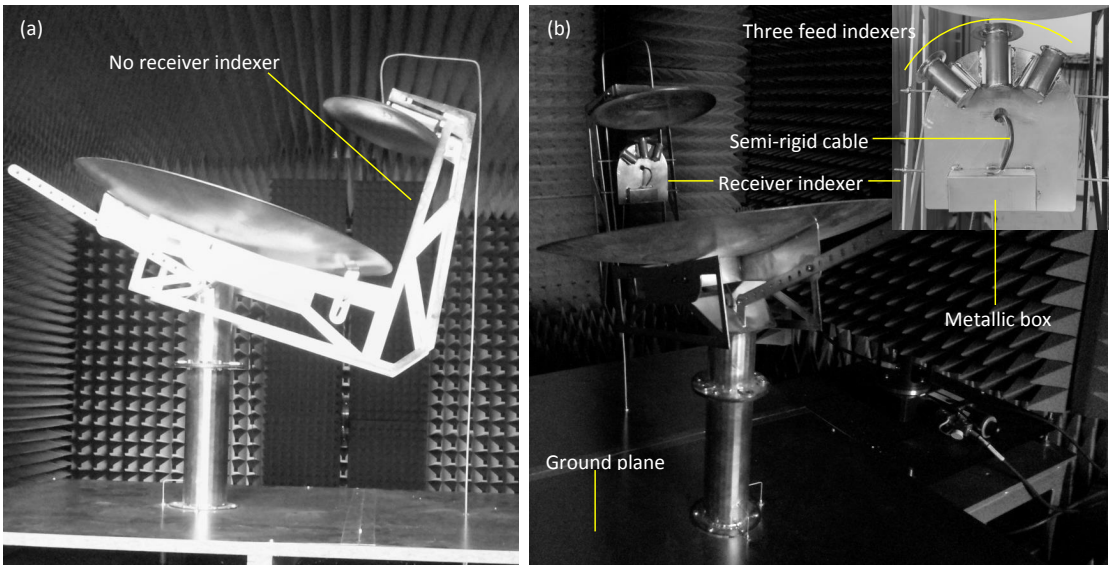

Figure 3.9: (a) Simplified MeerKAT scale model without the RI (b) Scale model with the simplified section of RI.

This semi–rigid cable runs through the connecting structure and enters the top of the foundation rod where it extends to the ground plane. The semi–rigid cable represents

a worst case cable shield running to the pedestal without any bonding. Thus induced currents from fields are expected to show a worst case coupling. Below the ground plate is a Sub–miniature version A (SMA) connector which is joined with the semi–rigid cable to create one of the ports that is used for S–parameter measurements. The metallic box represents shielded electronics behind the receivers on the actual MeerKAT dish.

A wire loop that was created on the inside of the pedestal is the stub–up section. The wire is attached to the SMA connector below the ground plate and soldered on the internal wall of the pedestal rod to form the pick–up loop. Figure 3.10 shows part of the ground plate when the complete model is unmounted. At the periphery of the pedestal ring are the screw holes. The central hole is the port that connects to the RI and the adjacent one forms the port for the stub–up. Ports 1, 2 and 3 were already in the early model. The additional ports for RI and stub–up allows for characterization of these parts. All the construction work and soldering of these two components (RI and stub–up) of the MeerKAT scale model were done at our engineering mechanical workshop.

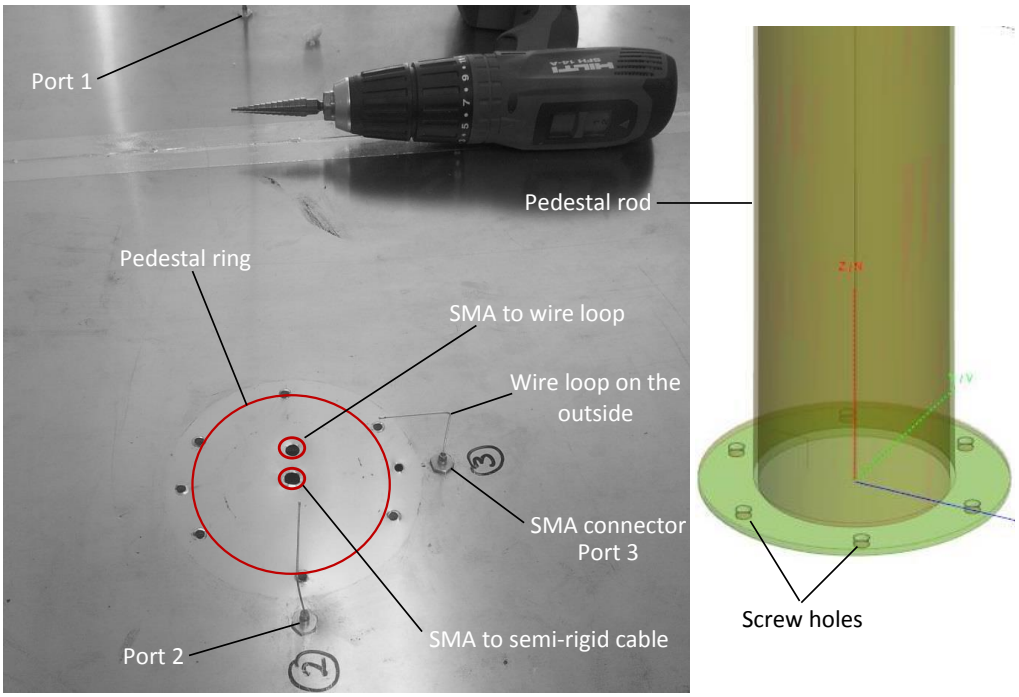

Figure 3.10: Section of the ground plane where the foundation rod is mounted. SMA connectors through the two holes inside the pedestal ring are attached to the wire loop and the semi–rigid cable independently.

3.3.4 FEKO Scale Model

An exact CEM model of the physical mock–up described in the previous subsection was modified in FEKO: That scale model is presented in Figure 3.11. Also shown are the full

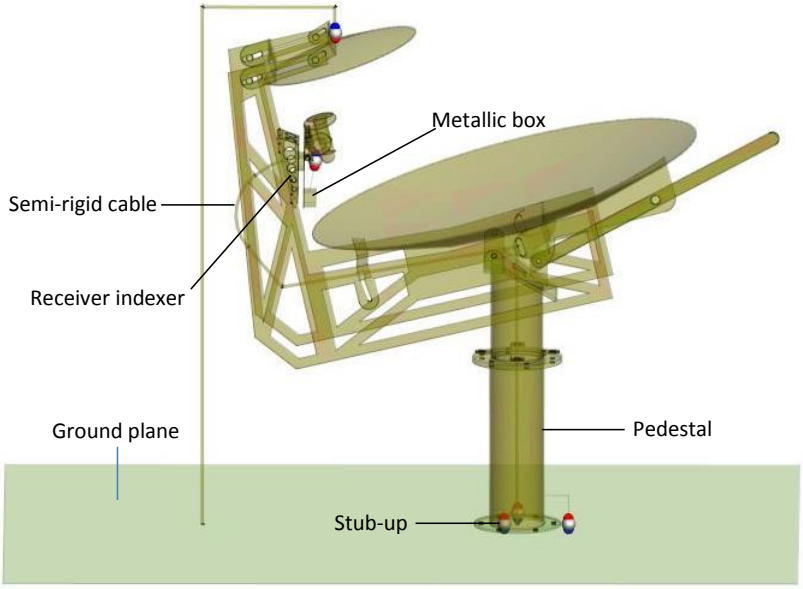

Figure 3.11: A simplified FEKO scale model with the RI and the wire loop (stub–up).

scale model of the RI and its components according to South African SKA mechanical design (Figure 3.12 (a)) and the $1/20^{th}$ scale model (Figure 3.12 (b)). The simplification of the RI was done to reduce the electrical size of the structure and to speed up simulation runs in FEKO.

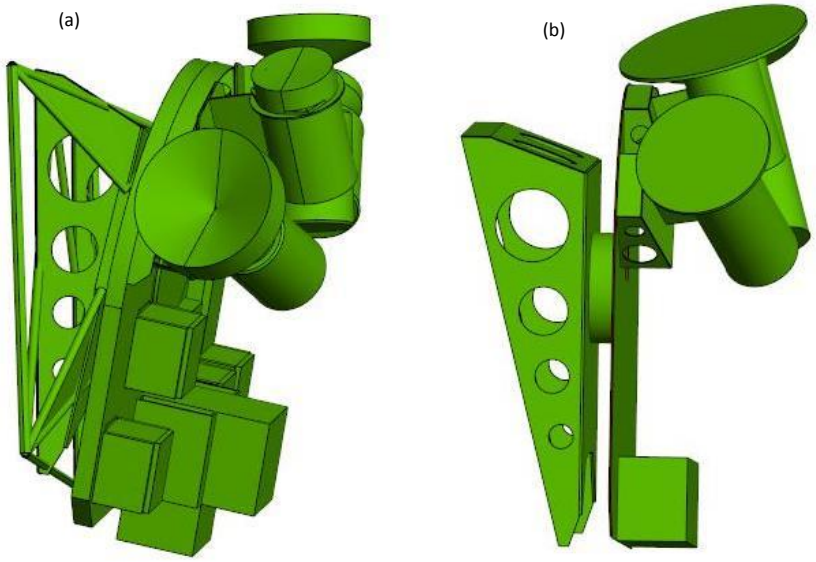

Figure 3.12: (a) Full scale mechanical design of RI and its various elements (a) Simplified $1/20^{th}$ of the RI model.

3.4 Verification of FEKO Scale Model

As pointed out earlier, the primary objective is to have a fully modified FEKO model which has been verified for characterization of RF coupling on the MeerKAT structure. This section explains how the modified $1/20^{th}$ scale model is used to validate the exact CEM model. The section has been divided into three subsections where the first and the second subsections describe lab measurement and FEKO simulation, respectively. Validation of FEKO model with measurement is discussed in the last subsection. Figure 3.13 shows the scale model inside an anechoic chamber and the CEM model in FEKO modelling environment.

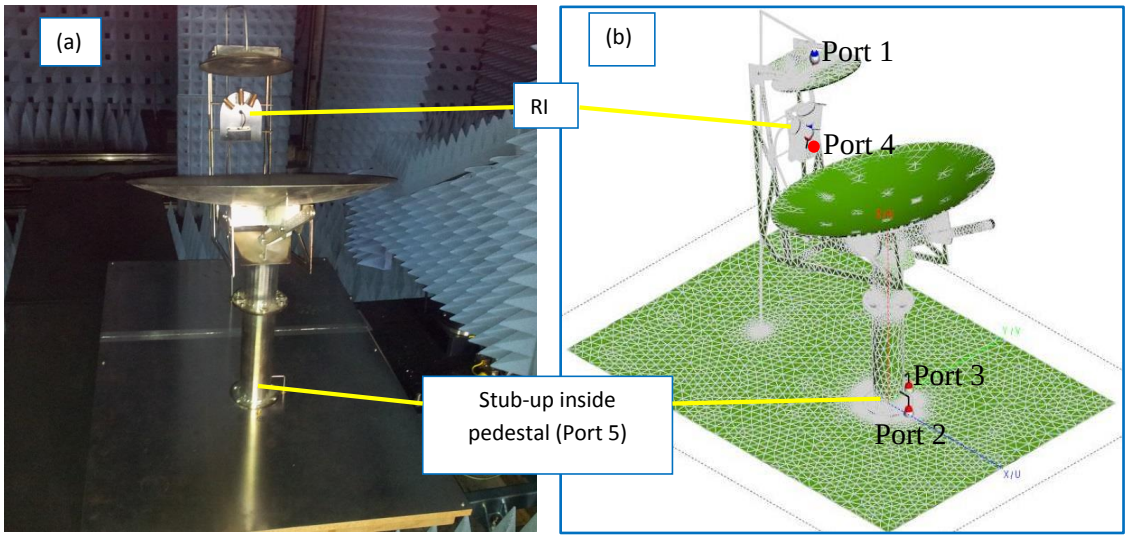

Figure 3.13: (a) Scale model inside anechoic chamber (b) Computational electromagnetic (CEM) model discretised in the Method–of–Moments (MoM) based code FEKO.

3.4.1 Lab Measurement

A Hewlett Packard two–port VNA was calibrated and together with the chamber were used for S–parameter measurements on the scale model. The method used for calibration was a short–open–load–through (SOLT) procedure. The measurements were taken from 45 MHz to 3 GHz with 201 frequency points. This range of frequency was chosen based on the range limited by the computational cost of modelling in FEKO, especially the upper frequency value. Nonetheless, the choice for lower frequency was a matter of preference to characterize the model from lower frequency values below the chamber's absorption limit. For close coupling the results are acceptable below the chamber absorption frequency, however, this is not the case with plane wave antenna measurements like in section 3.2.

In addition to the three ports that were used in the initial model [45], two more ports were included due to the retrofitting of the RI and the stub–up as explained in subsection 3.3.3 of this chapter. The adjacent FEKO model shows all the 5 ports that were utilised in the port definition. For each two–port VNA measurement, the unused ports were terminated with a 50 ohm load for comparison to the FEKO simulation where all the ports were defined as 50 ohm. S–parameter measurement between any pair of ports results into precise definition of both ports' reflection parameters, S_{11} and S_{22} as well as the transmission coefficients S_{12} or S_{21} which describe the extent of coupling. These S–parameters are compared with those from simulation in FEKO.

3.4.2 FEKO Simulation

The verification of the FEKO model (Figure 3.13 (b)) was done with scattering parameter measurements described in the previous subsection. The five ports were fixed with a 50 ohm impedance and were used to calculate S–parameters corresponding to the VNA data. The CEM model was discretised in the MoM based code FEKO. MoM was used extensively and successfully in EMC studies for KAT–7 [43]. However, the technique is computationally expensive in terms of both runtime and memory usage as the electrical size (complexity) of the problem increases. As an example, early computational results in section 3.2, took at least 10 days for a complete run in Babbage which has 12 cores and 256 GB RAM. Repeated for convenience, there were 64,459 discretised triangles in those simulations and 100 frequency points from 45 MHz to 3 GHz.

Therefore, since the current model was modified by additional parts, finding a way of reducing the computational time and the usage of a higher memory machine was very necessary. In this regard, the simulation files were submitted to the Centre for High Performance Computing (CHPC) in Cape Town, South Africa. The CHPC utilises the concept of *"division of labour"*; as would be described by an economist. Here, the solver load is distributed by way of parallel processing to various machines in a cluster environment. This parallelization is done through the message passing interface (MPI) or OpenMPI [48]. The MPI and OpenMPI are used for inter–node and intra–node communications respectively. The graphics processing unit (GPU) is used as well to further reduce simulation runtime. In this particular case, five nodes with a total of 500 GB of memory were used.

Another approach that was employed to accelerate simulations, was on the meshing process. Instead of discretising the model over the entire frequency range (45–3000 MHz) for 100 frequency points; meshing was done with different range of frequencies. Each

range had 20 frequency points, resulting into five simulation files for the same model. The lower frequency components had 97,037 discretised triangles while the higher components resulted into 129,846 triangles. The execution time was reduced by almost half that of higher frequency values. The calculation for each frequency point took approximately three hours; consequently, an upper frequency limit of 1.2 GHz was chosen.

3.4.3 Model Verification by Measurement

The comparison of the measurement and FEKO simulation are shown in Figure 3.14 to Figure 3.16. Since the simulation was limited to a higher frequency of 1200 MHz, only the frequency range of 45–1200 MHz from measurement data is used for verification purposes. The reflection coefficient S_{11} comparison gives the best correlation between measurement and FEKO results. The differences between the values are within 0.2 dB except for sections with resonances. This is attributed to minor differences in dimensional lengths in FEKO. Therefore, precise definitions of such lengths is required.

Figure 3.15 gives the magnitude of forward transmission gain (S_{21}) for ports 2–1 while Figure 3.16 shows the magnitude of S_{21} for ports 4–1. The results show a close agreement across the band; the difference between the computational and measurement data being less than 5 dB. The missing resonances by FEKO in both plots is due to the fewer number of frequency points calculated.

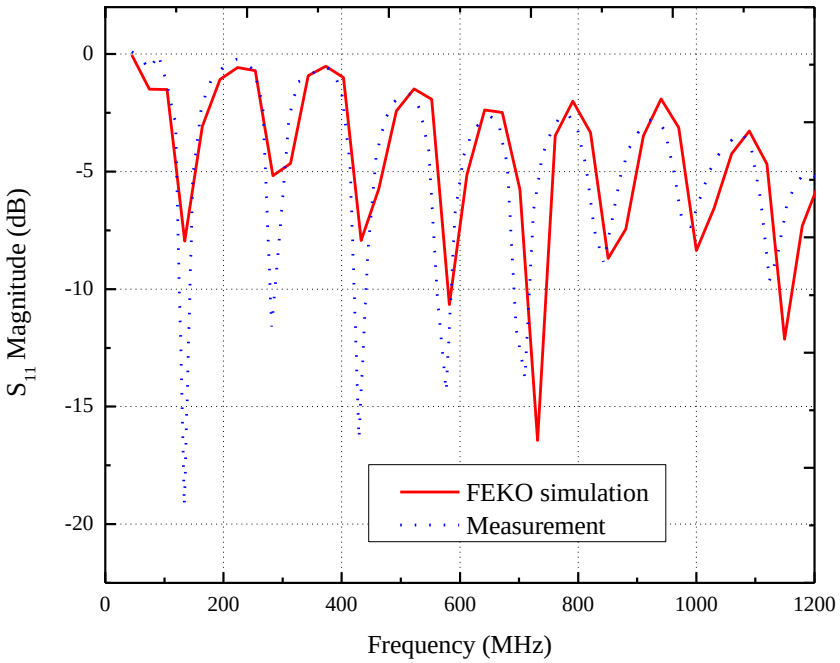

Figure 3.14: Comparison between FEKO simulation and measured results for S_{11}.

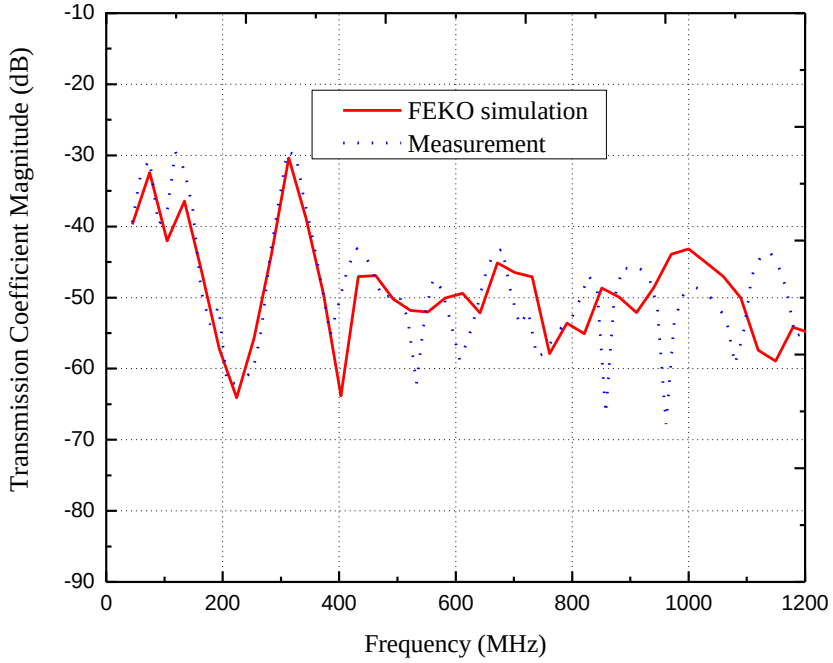

Figure 3.15: Comparison between FEKO simulation and measured results for S_{21} for ports 2–1 (old ports).

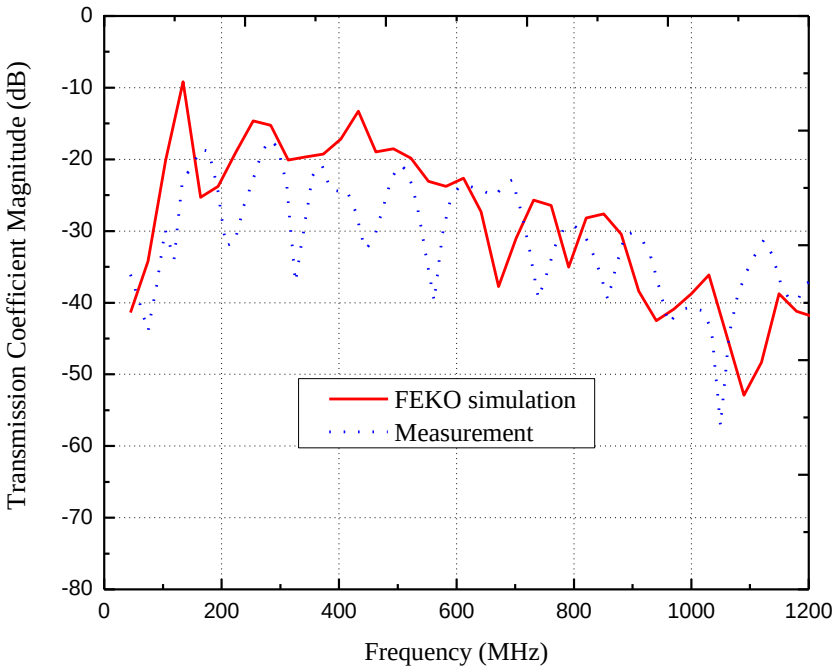

Figure 3.16: Comparison between FEKO simulation and measured results for S_{21} for ports 4–1 (new ports).

3.5 Summary

The initial MeerKAT scale model has been successfully characterized and retrofitted with core areas of interest; the receiver indexer and the stub–up. The key objective for the work described in this chapter, which is the validation of the modified CEM model, has been achieved with success. Detailed S–parameter measurements of the final scale model in an anechoic chamber, together with FEKO results, provides confidence on the MoM code. Nonetheless, the code needs to be evaluated further with on–site measurements before being fully utilized for rigorous coupling studies. This is discussed in the next chapter.

—What we need is not the will to believe but the will to find out —

—Bertrand Russell —

CHAPTER 4

Coupling Fields on the MeerKAT Structure

The coupling levels of currents on the structure cables even from low level radiated fields from the neighbouring sensors can potentially cause RFI. We quantify the levels of coupling on the actual MeerKAT dish by inducing currents from known radiator fields. The verified CEM model in the previous chapter is illuminated with a plane wave (as a source of known field) to generate segment currents. Taking into account the effects of ground reflections and path losses, the received E–field together with the induced currents on the MeerKAT structure are used to determine a transfer function parameter (TF). This parameter is used to compare results from on–site measurements and simulation. With confidence the validated FEKO model can now be recommended for rigorous RFI coupling studies.

The first section of this chapter describes on–site measurement procedure where an emission reference source, current probe and a spectrum analyser are used for data collection. It also discusses field measurement results of induced currents on structure cables. The second part of the chapter validates the free space path loss equation with simulation from FEKO and then focusses on the discussion of results from Karoo measurement and CEM modelling.

4.1 On–site Measurements

Karoo measurements are very important not only for intrinsic gain in terms of hands–on experience with measurement procedures but also for actual data collection. It gives another dimension of dealing with measurements which contributes to a refined approach to computational modelling. However, organizing for such measurement campaigns involve much time and effort. Therefore, any slightest opportunity given for measurement is a golden chance that is optimally utilized.

This section describes the measurement set–up in the field and the specific equipment used for our coupling investigations. Thereafter, discussion of the results are presented.

4.1.1 Measurement Procedure

In order to qualify the shielding effectiveness with RF coupling on the MeerKAT structure, a standard radiator (operating from 30 MHz to 1 GHz) was used as a source of radiated interference and measurement of the coupled RFI was carried out on the dish itself. With the front part of the MeerKAT telescope facing in the Eastern direction as shown in Figure 4.2 (a), an emission reference source (ERS) was placed 30 m to the North of the dish. Figure 4.1 gives a plot of radiated fields from the ERS when vertically polarized and the adjacent photo is the ERS radiator.

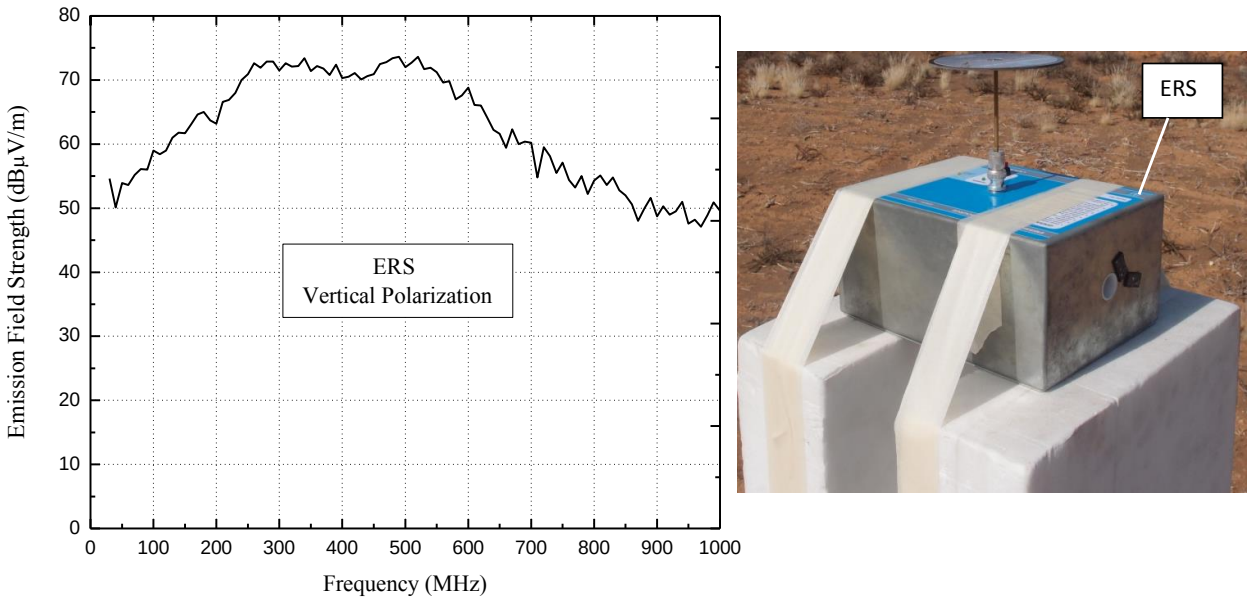

Figure 4.1: A plot of vertically radiated E–field from ERS and to the right is the equipment itself.

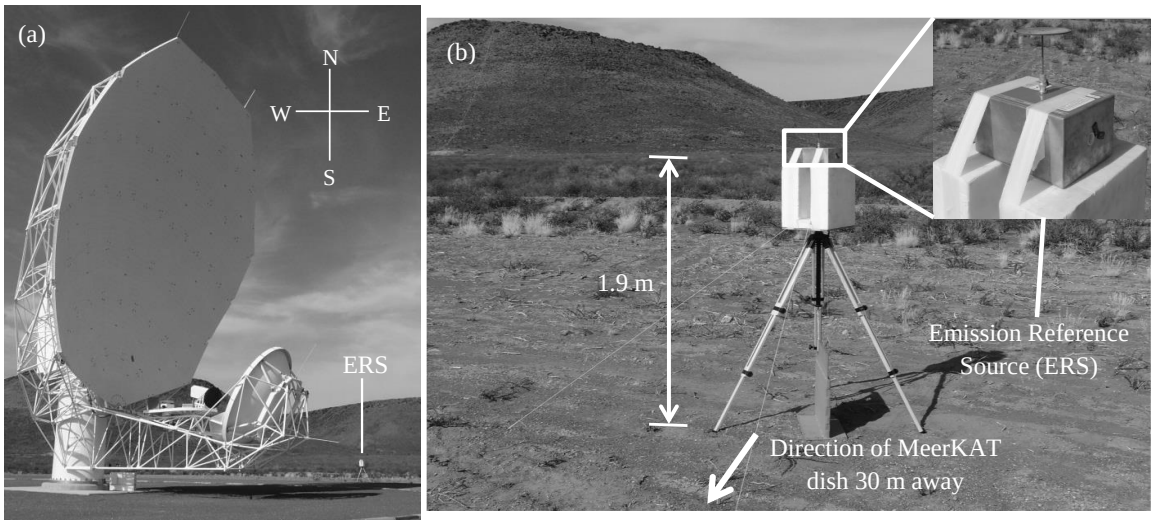

Figure 4.2: (a) Front section of the MeerKAT facing in the Eastern direction. At the background is the radiator. (b) ERS radiating at a distance of 30 m away from the telescope. Inset: Zoomed view of ERS.

The reflectors were tilted down to a minimum level where the RI of the antenna was 3.2 m above the ground. This made it possible for ease of access to the cables above and below the RI for data collection. For safety reasons or due to the sensitivity of the MeerKAT antenna, we had a small window of measurement opportunity (four hours) and everything had to be switched off except the equipment used for measurement. A metallic cap was used to shield the receiver until all the scheduled measurements were completed. The ERS was mounted on a tripod stand, 1.9 m off the ground as presented in Figure 4.2 (b). A current probe together with a hand–held spectrum analyser (FSH4 SA) were used to measure the background noise (ERS switched off) before the measurement of RFI levels on selected cable points as in Figure 4.3 (bottom right photo).

All the equipment to be used at the Karoo site were first tested at the SKA reverberation chamber to qualify them for use at the site. Nonetheless, it was still necessary to verify that the E–field from the ERS was not strong enough to interfere with nearby KAT–7 operations. Therefore, a 20 dB and 10 dB attenuators were connected to the ERS separately to ensure a low and gradual increase of the E–field radiated. However, there were no significant spikes registered above the noise floor on the FSH4 SA. Consequently, the ERS was used directly without any attenuator connected.

Figure 4.3: Top: Full MeerKAT dish with pedestal door opened. Bottom left: Measurement of induced currents on the earth stub–up within the pedestal. Bottom right: Measurement of RF levels on the cables below the RI using current probe and spectrum analyser.

Tests were done on various cables around the RI region and the earth stub–up inside the pedestal (Figure 4.3 (bottom left)). Within the pedestal is the shielded drive compartment (SDC), which is an integral part of the antenna tower that houses control electronics of the telescope. Access to the SDC is through an RF sealed door inside the pedestal, therefore, the pedestal main door is not sufficiently shielded as the SDC door. As a matter of interest measurements were taken with the pedestal door closed and then repeated with the door opened for comparison of induced fields.

4.1.2 Magnitude of Current on the Cables Inside the Pedestal

The results for the measurements done on the earth cable in the stub–up and the emission box connector cable within the pedestal chamber are shown in Figure 4.4 and Figure 4.5 respectively. These are the actual magnitudes of currents after filtering out the effects of the background noise from the measured data.

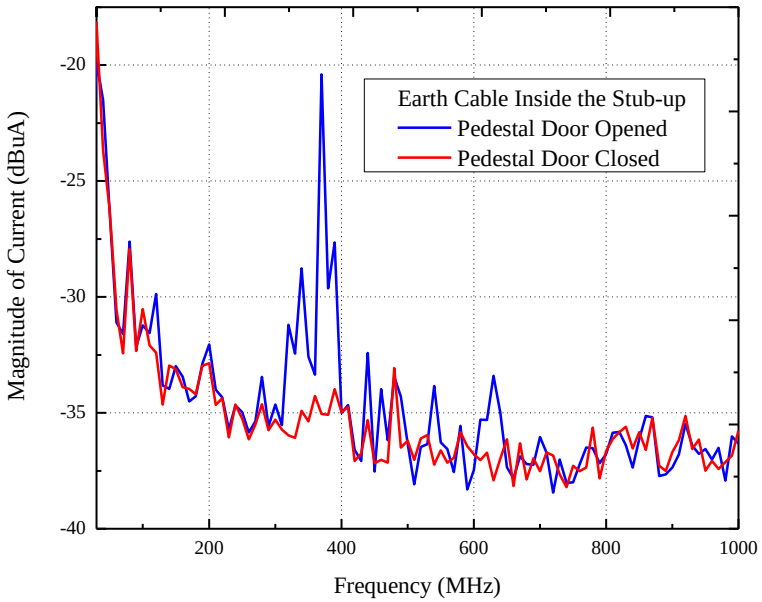

Figure 4.4: RF current levels on the stub–up earth cable with the pedestal door opened and closed.

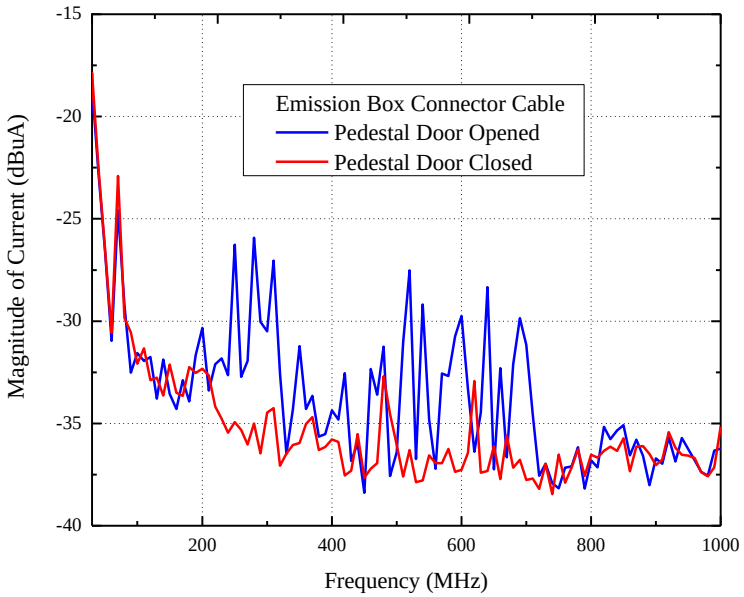

Figure 4.5: RF current levels on the emission box connector cable with the pedestal door opened and closed.

From Figure 4.4, there are noticeable spikes between the frequencies 300–650 MHz where the signal current levels with the pedestal door opened are higher than when the door is closed. The easily noticed spikes are within 300–400 MHz range where the maximum difference in the magnitude of currents for the two cases (door opened and closed) is 12.8 dBμA. A few that can be singled out between 400–650 MHz give a slight difference of 2.5 dBμA. The effect of leaving the pedestal door open is much more pronounced in Figure 4.5 where the interference levels are within a wider frequency range of 200–720 MHz. The difference in the signal levels is approximately 9.9 dBμA within that frequency range.

From the results, it appears that the pedestal door is providing some shielding. However, it is difficult to quantify the level of shielding provided by the door due to possible effects of EM modes that can develop inside. Only certain frequencies show effect, which is on a wider range for emission box cable than earth stub–up. Therefore, conclusions cannot be drawn from these preliminary results which require further studies because of uncertainties of mode coupling.

4.1.3 Magnitude of Currents on the Cables Around RI

As mentioned earlier, the cables that run to the RI section of the MeerKAT are connected to the shielded electronics behind the sensitive receivers. Therefore, it was important to investigate the RF coupling levels on this cables using simulated fields (ERS emissions). This was achieved by measuring induced currents on the cables that were easily accessible using current probe and FSH4 SA (Figure 4.3 (bottom right photo)).

The impact of the ERS radiated field levels (refer to Figure 4.1) on different cables around the RI are depicted in Figure 4.6 and Figure 4.7. The coupled currents on the limit switch and the motor cables are dominant over those of the signal and signal distribution box cables almost in the entire frequency range. It is only the limit switch cable which has most of the spikes above -15 dBμA between 240 and 580 MHz, followed by three spikes for the motor cable and each for the remaining cables. This is attributed to different bonding paths of theses cables hence different sizes of pick–up loops formed which will in–turn influence the magnitude of the induced field. Just as in the previous plots, it can be noted that the highest RF coupling levels is within 200–400 MHz frequency range except for the limit switch cable whose values extend up to 600 MHz.

The overall results in this section show that below -35 dBμA there are no sharp spikes which is a characteristic of an absence of induced interference. Therefore, it is possible that below this value we are only measuring the noise floor of the receiver system (FSH4 SA). In summary, the magnitude of these currents are very low and the individual cables

have different coupling levels depending on the length between earth bonds and placement. Therefore, field measurements and CEM modelling need to be combined for realistic predictions of coupling levels. This is channelled into the next section with detailed computational analysis to supplement on–site measurements.

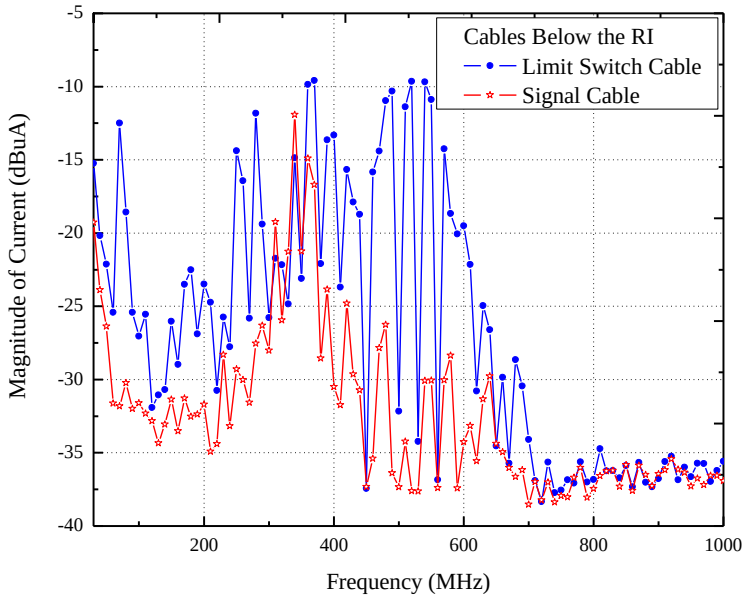

Figure 4.6: Magnitude of the current levels on the limit switch and the signal cables below the receiver indexer.

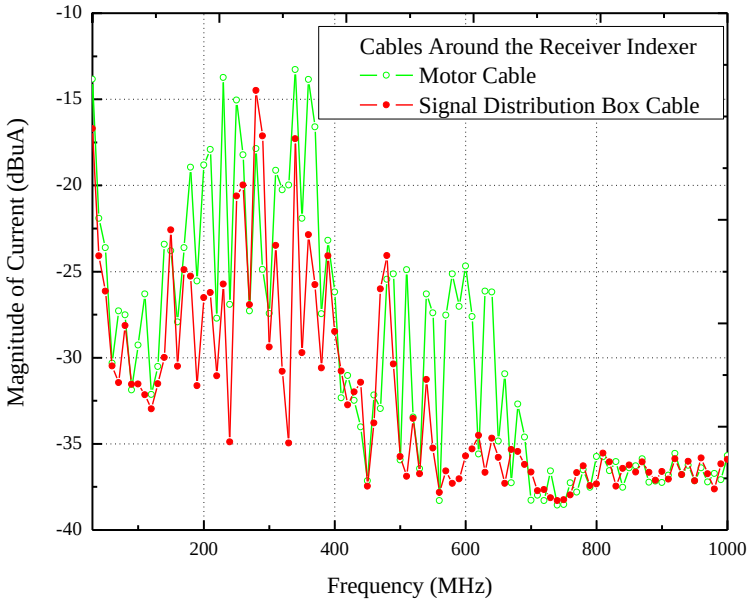

Figure 4.7: Magnitude of the current levels on the motor and the signal distribution box cables above the receiver indexer.

4.2 Karoo Measurement and FEKO Simulation

The Karoo measurement procedure that is well described in subsection 4.1.1, presented us with valuable data of induced potentials on the actual MeerKAT structure due to the ERS vertical E–field (Figure 4.1). The task was to find a parameter that can be used to compare field measurements and FEKO simulation. Taking the following into consideration:

- Effects of ground reflections and path losses
- That we already had the data for radiated E–field and induced potentials
- It was easy to define a plane wave that illuminates FEKO model and to request for segment currents

A transfer function (TF) was defined and utilized to evaluate on–site measurement with computational modelling.

$$TF = \frac{E_{rec}\ \text{(V/m)}}{I\ (\mu\text{A})} \tag{4.1}$$

where E_{rec} is the incident electric field just at the MeerKAT antenna while I is the current on a wire segment in the computational model. The units of TF are in dB$\mu\Omega$/m derived from the individual parameter units in equation (4.1). For the actual measurements, the RF current (I) in micro–ampere in the cable under test is determined from the reading of the current probe output (V) in microvolts divided by the already known probe transfer impedance (Z_T).

$$I = \frac{V\ (\mu\text{V})}{Z_T\ (\Omega)} \tag{4.2}$$

It is expected that the incident E–field received by the antenna to be less than the field radiated by the ERS due to free space path loss (FSPL) and ground reflections (GR). Therefore, the exact E–field at the tested cables is computed using the ERS calibrated data and the FSPL described in the following subsection.

4.2.1 Validation of Free Space Path Loss (FSPL)

The data from calculated FSPL using the free space loss equation was utilised to verify FEKO simulation results. In the log domain, the *loss* equation is expressed as [53]:

$$fspl = 20log(f) + 20log(d) - 27.55 \tag{4.3}$$

where f is frequency in MHz and d is the path length in metres. The frequency range, 30–1000 MHz, from the actual measurement and the path length, 30 m, are used in Matlab to obtain the FSPL values.

For simulation set–up, two perfect electric conductor (PEC) dipoles of size 0.0625 m are defined without the ground plane (homogeneous free space medium) as in Figure 4.8. This value is calculated based on the highest frequency value 2,400 MHz discussed in subsection 4.2.2. However, any size of the dipole can be used as long as their heights from the ground are well defined. The first dipole is 1.9 m off the "ground" and the other is 3.2 m above the same surface. They are vertically polarized and separated by a distance of 30 m like in the real measurements. The S–parameters are requested for the computation of the FSPL since they are related through Friis transmission equation [16, 54, 55]. From Figure 4.9 the required transmission coefficient is S'_{21} which gives the loss factor due to the surrounding medium. Nonetheless, FEKO computes the S_{21} which is given by the square root of the ratio of output power (P_{out}) to input power (P_{in}). However, the ratio of interest is the received power (P_{rec}) to radiated power (P_{rad}). Considering Figure 4.9 as a linear system of nodes and branches in series, with only one incoming (P_{in}) and one outgoing (P_{out}) wave, then the FSPL or S'_{21} can be obtained through equation (4.4) [16]:

$$\text{FSPL} = |S'_{21}|^{-2} = \frac{P_{rad}}{P_{rec}} = \left[\frac{|S_{21}|^2}{(1-|S_{11}|^2)(1-|S_{22}|^2)}\right]^{-1} \tag{4.4}$$

where the S–parameters, S_{11}, S_{22} and S_{21} are attained directly from simulation. A similar configuration as in Figure 4.8 was used but with an infinite ground plane (see Figure 4.10). The PEC ground plane takes into account the worst case reflections from the ground.

Figure 4.8: Simulation of S–parameters using two dipoles for FSPL calculation.

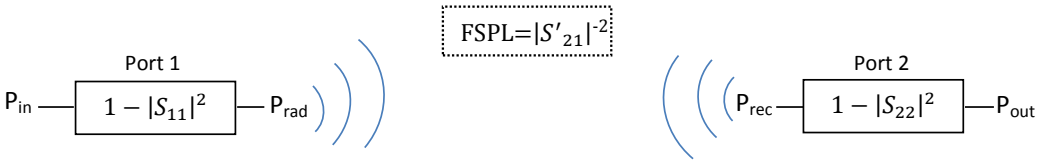

Figure 4.9: Simplified illustration of how two dipoles with defined ports are used to obtain S–parameters for the determination of FSPL.

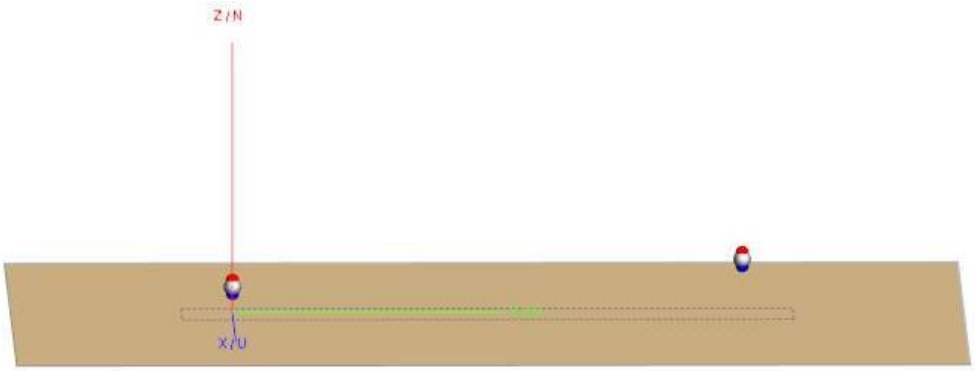

Figure 4.10: Two dipoles with a PEC ground plane for the computation of loss coefficient, S'_{21}, taking worst case ground reflections into account.

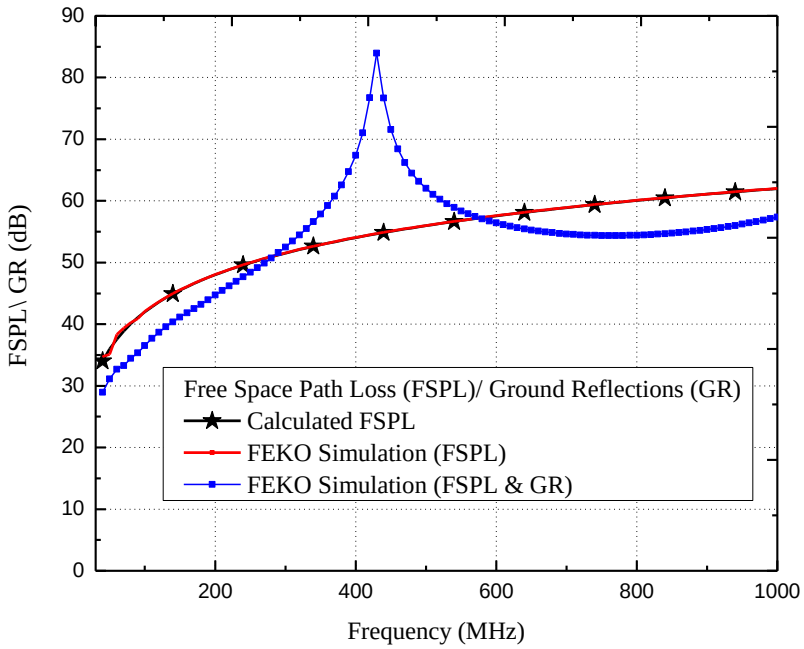

Figure 4.11: Comparison of FSPL and GR for the calculated values and simulation.

Figure 4.11 shows the result comparison of FSPL from simulation and the computed values from the loss equation. The plot for FSPL–GR is only from FEKO simulation. The graphs for FSPL from the code FEKO and calculated data give a similar trend and a

perfect match across the entire frequency band. Friis Transmission equation is used for direct line of sight predictions, whereas FEKO takes difference in height into account. The FSPL–GR plot predicts less losses except at 420 MHz. This is due to reflected signals from the PEC ground adding out of phase with the direct signals incident at the antenna, so they cancel and as a result lead to more medium *loss* and less received power at the antenna. However, at about 800 MHz the signals add in phase, which would "double" it i.e. 6 dB less medium *loss*. The difference between simulated FSPL and FSPL–GR is within 5 dB. Therefore, the impact of the real ground (Karoo soil) reflections would be less than 5 dB compared to FSPL. Since the meshing of the dielectric medium for the Karoo soil leads to more computational time, only the verified FSPL is used in determining the E–field that couples into the MeerKAT cables.

4.2.2 The Use of Verified $1/20^{th}$ CEM Model for RF Coupling Investigations

Before any simulations could be done, it was important to ensure that the CEM model was in the same orientation as the actual dish (Figure 4.3) and that there was a radiated field incident on the model (as in the real case in Figure 4.2). In that regard, our verified FEKO model was tilted and illuminated with a plane wave (see Figure 4.12) to depict the set–up in the field. After this it was now a matter of carrying on with other simulation procedures to generate the induced currents that will be used in determining the TF described at the beginning of this section. The TF will in turn be used to compare results from measurement and FEKO simulation.

The E–field of the approaching signal was 1 V/m and vertically polarized. A frequency range of 600–2400 MHz was used in the MoM code for meshing and corresponds to 30–120 MHz in full scale terms. The lower frequency limit was basically the lowest operational frequency for the ERS while the upper frequency limit was chosen to be within the memory available in computations facility available named Babbage. Two wires which are connected from the ground plane to the metallic box behind the receivers are shown in Figure 4.13. The wires represent the cables that route to the receiver indexer and through them we obtain the requested wire segment currents. These element currents together with the E_{rec} of the FEKO model are utilised to calculate the TF.

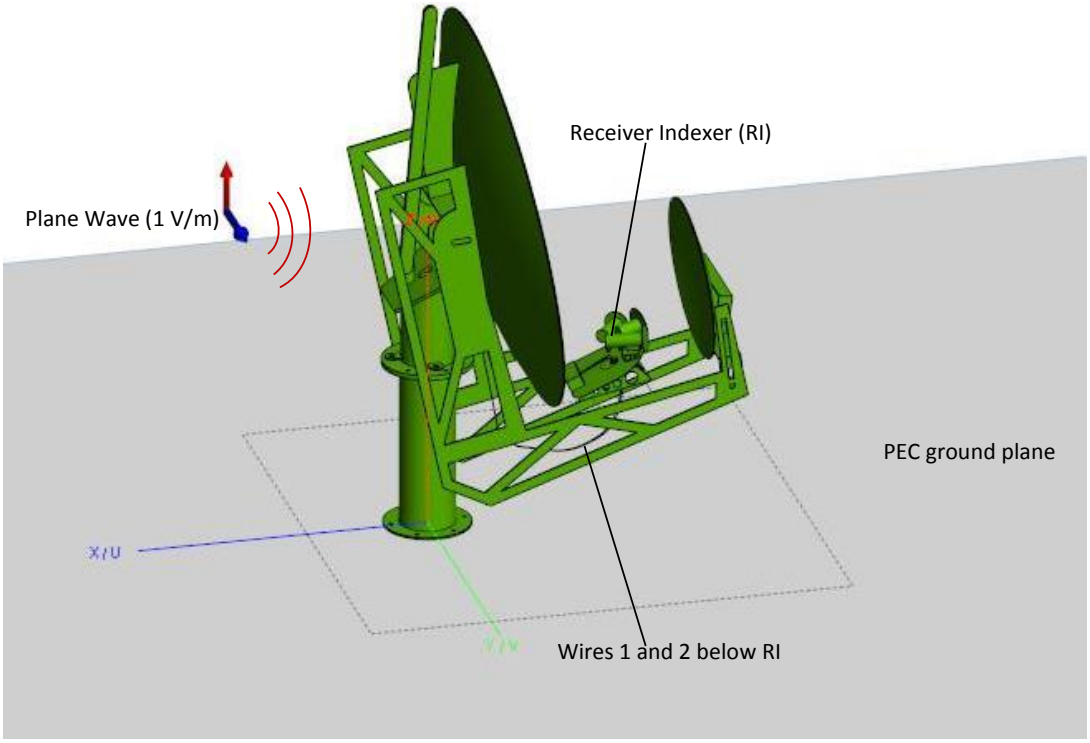

Figure 4.12: Plane wave of magnitude 1 V/m incident on the MeerKAT model.

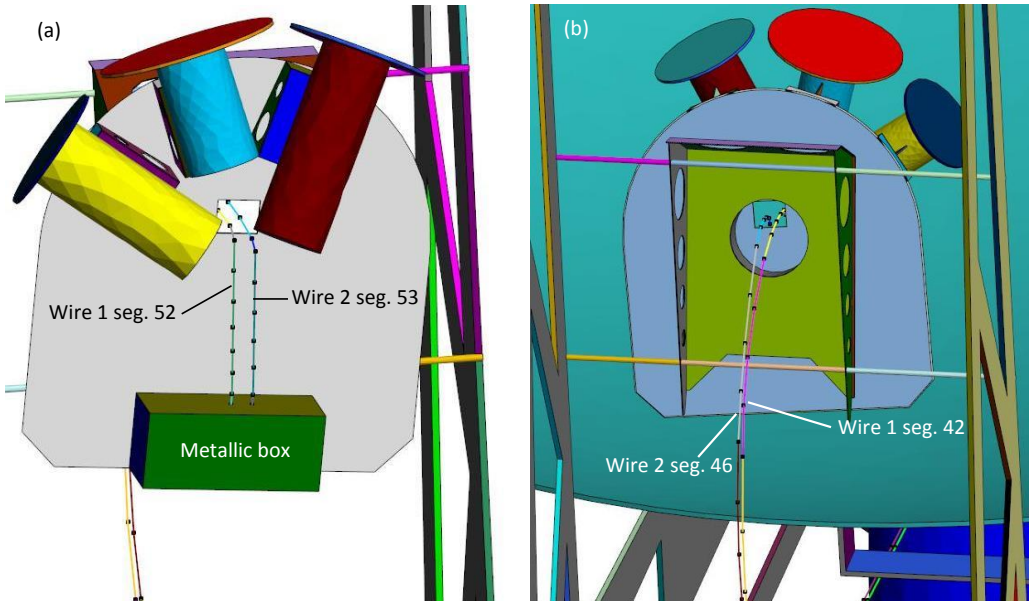

Figure 4.13: (a) Top view of RI showing two wire segments, 52 and 53 (b) Bottom view of RI with different segments for wire 1 and wire 2.

It was then possible to compare the transfer function from simulation to that of the measurement once the E_{rec} was computed from the known radiated field together with the FSPL from subsection 4.2.1. In linear terms E_{rec} is given by the following equation:

$$E_{rec} = \frac{E_{rad}}{\sqrt{FSPL}} \tag{4.5}$$

where E_{rad} is the radiated field by ERS (data from calibration).

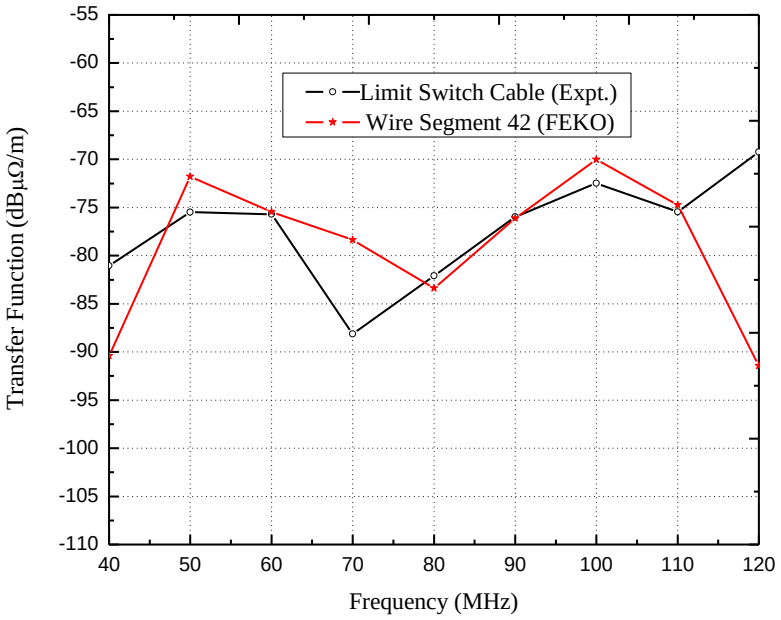

Figure 4.14: Result comparison of transfer function due to coupling currents on the limit switch cable on the actual MeerKAT dish and wire segment 42 on the FEKO model.

Figure 4.14 shows a good comparison between simulation and measurement for the values of TF. The plots are not in precise alignment because the wire segment 42 (Figure 4.13 (b)) where the currents are requested does not represent the exact position where the current probe was placed on the limit switch cable for RF coupling measurements. The difference in the results is within 5 dB$\mu\Omega$/m except at 40 MHz, 70 MHz and 120 MHz frequencies.

Further comparison of results was done on the earth stub–up between simulation and measurement. From Figure 4.15 the two graphs tend to have a similar trend until 90 MHz frequency. The average value of the transfer function for the difference in the two plots is 11.2 dB$\mu\Omega$/m. This large difference between simulation and measurement is expected because the cavity sizes (for CEM model and actual dish) do not scale exactly. That is to say, in the CEM model the stub–up section has been simplified as a wire loop that only gets shielded by the pedestal rod while the remaining part of the cavity is basically empty. However, in the actual MeerKAT dish there are different partitions such as the SDC and the stub–up itself (refer to Figure 3.8) which may set up different EM modes as mentioned in subsection 4.1.2.

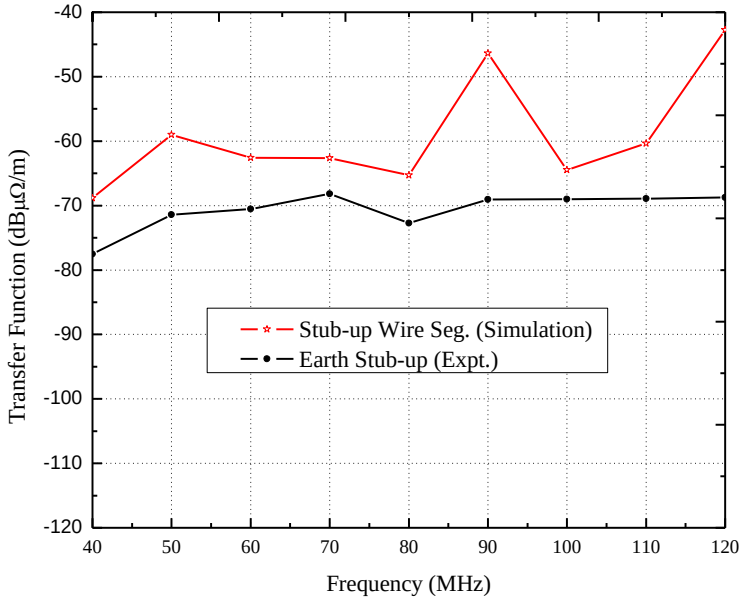

Figure 4.15: Comparison between measurement and simulation results of transfer function due to currents on the earth stub–up.

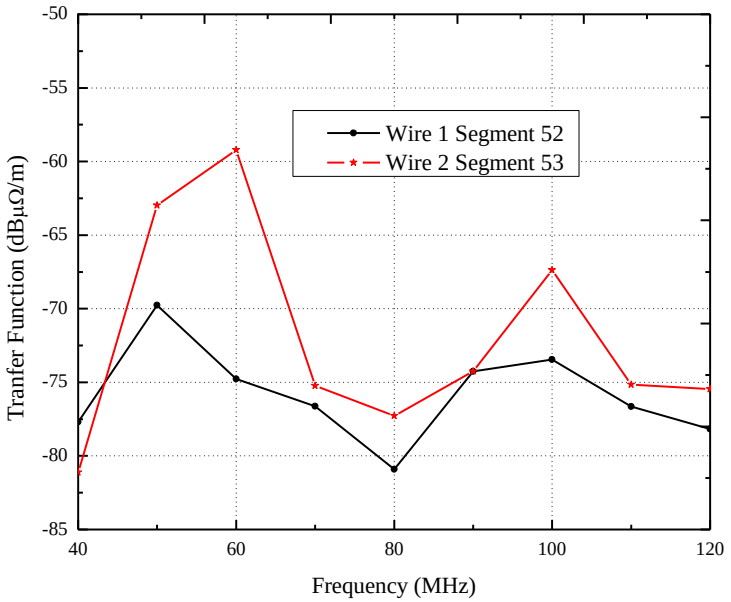

Figure 4.16: Comparison of transfer function of wire 1 segment 52 and wire 2 segment 53.

The graphs in Figure 4.16 give the transfer function of two segments, 52 and 53 of wire 1 and wire 2 respectively (refer to Figure 4.13 (a)). The objective is to compare the coupling of currents on the two segments which are almost at the same point but in two different wires. From the plots, there are differences in the magnitude of the transfer function of the two segments due to different coupling levels of currents. Even though both wires in the CEM model are connected to the same metallic box and the ground plane, they have

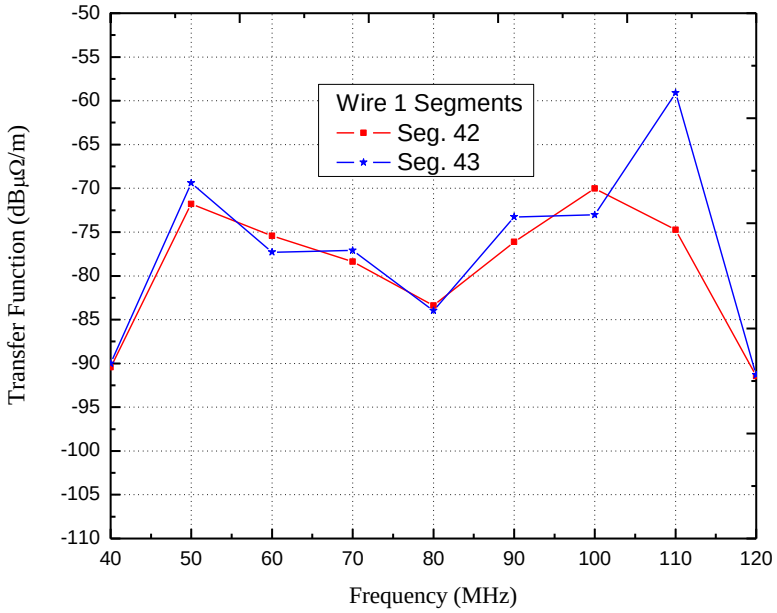

Figure 4.17: Comparison of transfer function of different segments on same wire.

slightly varying lengths. The variation in length was due to displacement of wire bends which as a result leads to varying RF coupling levels in different wires.

The comparison of transfer function for segments 42 and 43 on wire 1 is presented in Figure 4.17. There is a good correlation in the plots which implies that the magnitude of the induced segment currents on same "wire 1" is the same. However, the cause for the 15 dB difference at 110 MHz was not known. A possible reason could be a computational error associated with the meshing of that segment or some error that requires further investigation.

4.3 Summary

This chapter has discussed in detail on–site measurements of induced currents on structure cables of the actual MeerKAT telescope. An emission reference source (ERS) with known fields together with a current probe and a spectrum analyser were used to investigate coupled currents on different cables around the receiver indexer (RI) and earth stub–up inside the pedestal. As highlighted in chapter 3, part of the research was to study RF coupling levels around these two critical parts of the antenna (RI and the stub–up). This has been achieved not only through actual measurements in the field but also through computational modelling.

The verified FEKO model has been used effectively to evaluate our on–site measurements

by use of a transfer function parameter. With confidence the validated CEM model can now be used for further coupling studies of MeerKAT telescopes. However, minor improvements on the model as mentioned in the recommendation chapter is still important for faster and more efficient results.

—Keep on going and the chances are you will stumble on something, perhaps when you least expect it. I have never heard of anyone stumbling on something sitting down —

—Charles F. Kettering —

CHAPTER 5

Conclusions and Recommendations

A review on the major concepts of radio telescopes including the receivers and radio frequency interference (RFI) in radio astronomy is provided in chapter 2. The literature gives the major spectrum allocation of radio frequency (RF) bands in South Africa. It is apparent that not much spectrum allocation has been set aside for radio astronomy applications within these bands. Due to competition from commercial entities, an over–lap of the frequency bands is evident and as a result, RF from nearby adjacent channels pose a continuous threat to astronomical signals. The South African SKA has taken pro–active measures such as the identification of a radio quite zone, the Karoo site, and to ensure that RFI becomes an integral component of the electrical and mechanical design of the MeeerKAT antenna. The evident gap (coupling of nearby radiations into MeerKAT structure) has been filled with the findings from this research in terms of the efforts put by the SKA in the shielding of the telescope.

This dissertation has examined the technique for electromagnetic (EM) characterization of the MeerKAT structure. Particular focus has been on the receiver indexer (RI) region (which needed to be qualified in terms of cabling and shielding) and the earth stub–up region at the base of the pedestal. An extensive check on the verification of the computational electromagnetic (CEM) model using the scale model in an anechoic chamber has been attained. It is mentioned in chapter 2 that a similar approach was successfully used for lightning–induced RFI and earthing studies which led to original design contributions regarding lightning protection and the layout of galvanic systems for the present KAT–7

structures. Our verified MeerKAT CEM model is used in detailed investigation of RF coupling fields on the MeerKAT structure to approve its shielding effectiveness. However, the intention is not to use it in isolation for realistic predictions. There are two reasons that make this approach effective and convenient: firstly, on–site measurement opportunities come at a premium and with limited measurement time, and secondly, the construction of MeerKAT telescopes is still on–going. Therefore, the actual dish to dish coupling investigation is not possible at the moment which gives way for CEM modelling.

A Method of Moments (MoM) frequency domain CEM code, FEKO, was used in our RFI characterization of the MeerKAT structure. Due to large simulations required for the MoM code, we requested for assistance from the Centre for High Performance Computing (CHPC) in Cape Town, South Africa. Five nodes were made available for us with 500 GB of memory but still the simulations would take at least 3 days. Due to FEKO licensing issues at some point, time constraints of the research and CHPC not being available at the moment, our dish–dish coupling investigation (which require much memory) using the validated model was not viable. However, a standard radiator that was used as a source of RFI together with the MeerKAT antenna (M63) which has already been commissioned by the SKA provided a close alternative approach of coupling between the telescopes. With this, it was possible to study the induced currents on the cables with the pedestal door opened or closed. The verified CEM model was illuminated with a plane wave to replicate the scenario in the field.

On–site measurements quantify the levels of current that can be measured on specific cables around the RI and on the earth stub–up section. The RF coupling levels on these cables are as low as below -7.5 dBμA. A comparison of the field measurement and simulation is done by using a transfer function (TF) parameter. The best comparison gives a good agreement to within 5 dB. The evaluation of TF takes into account the free space path loss and neglects minor reflection from the ground. Generally, the results show that the contribution from computational analysis as a research tool agree well to practical measurements.

The verified simplified scale model used in CEM agree to real full scale dish measurements on–site. This provides confidence to use FEKO model for further investigations. For future studies, the following recommendations are put forth towards the realisation of similar goals:

- The use of emerging powerful hybridised FEKO solvers instead of MoM alone will reduce computational time considerably. Dish to dish coupling investigations using the validated FEKO model can be determined much faster.

- The FEKO model can be simplified further by focussing on the areas of importance and removing the other sections to reduce the mesh size. This does not require verification again but only re–meshing of the model.
- With an enclosed CEM model within a volume of space, the near–field pattern of the antenna structure can be requested and then be transformed so that the far field pattern can be obtained. This will give important information on the side lobe and main lobe gains for the RFI coupling investigations.

—No research will answer all queries that the future may raise. It is wiser to praise the work for what it has accomplished and then to formulate the problems still to be solved —

—Theobald Smith —

References

[1] I. Asimov, *Eyes on the Universe*. Andre Deutsch, 1975.

[2] A. Boonstra and S. V. der To, "Spatial filtering of interfering signals at the initial low frequency array (LOFAR) phased array test station," *Radio science*, vol. 40, 2005.

[3] S. Zaroubi, G. van Diepen, A. Offringa, A. de Bruyn, S. Daiboo, and G. Harker, "The LOFAR radio environment," Astronomy and Astrophysics, 2013.

[4] "The history of the SKA project." https://www.skatelescope.org/project/ history-of-the-skaproject.

[5] "Square Kilometre Array SKA Africa." www.ska.ac.za.

[6] H. Ott, *Electromagnetic compatibility engineering*. John wiley and Sons Inc., 2009.

[7] J. Jonas, "The South African Array with Composite Dishes and Wide–band Single Pixel Feeds," IEEE, Aug 2009.

[8] "Protection criteria used for radio astronomical measurements," International Telecommunications Union, Rec. ITU–R RA.769–2, 2003.

[9] G. C. Southworth, "Early history of radio astronomy," The Scientific Monthly, 1965.

[10] C. D. Pree and A. Axelrod, *The Complete Idiot's Guide to Astronomy*. Pearson Education Company, 2^{nd} ed., 2001.

[11] T. Macnamara, *Handbook of Antennas fo EMC*. Artech House Inc., 1995.

[12] C. Wang and T. Keech, "Antenna Models for Electromagnetic Compatibility Analyses," tech. rep., U.S. department of commerce NTIA, Oct. 2012.

[13] V. V. Bhargav, G. K. Mahanti, and B. C. Mahato, "Minimization of Side Lobe Level of Scanned Linear Array Antenna with Fixed Dynamic Range Ratio utilizing Iterative Fast Fourier Transform," IEEE, 2011.

[14] T. MVSR, A. Kumar, and C. V. Prasanth, "Comparative Analysis of Windowing Techniques in Minimizing side lobes in an Antenna array," International Conference on Communication and Signal Processing, April 2014.

[15] "Space research earth station and radio astronomy reference antenna radiation pattern for use in interference calculations, including coordination procedures," RECOMMENDATION ITU-R SA.509-2, 1978–1990–1998.

[16] D. M. Pozar, *Microwave Engineering*. John Wiley & Sons, Inc., 4 ed., 2012.

[17] J. D. Kraus, *Antennas*. McGraw–Hill Book Company, 1950.

[18] M. E. Tiuri, "Radio Astronomy Receivers," *Antennas and propagation, IEEE transactions*, vol. 12, pp. 930–938, 1964.

[19] R. Blundell and C. E. Tong, "Submillimeter Receivers for Radio Astronomy," *Proceedings of the IEEE*, vol. 80, November 1992.

[20] J. L. Steinberg, *Radio Astronomy*. McGraw–Hill Electronic science series, 1963.

[21] D. M. Pozar, *Microwave and RF Design of Wireless System*. John Wiley and Sons, Incorporation, 2001.

[22] "Proposal to site the SKA – Analysis of the Radio Frequency Environment," National Research Foundation, March 2006.

[23] "The South African Telecommunications Act (Act 103 of 1996)," Government Gazette.

[24] G. Beger and A. Sinha, "South african mobile generation: Study on south african young people on mobiles," *unicef*, May 2012.

[25] "Global Information Society Watch 2008," *APC, Hivos and ITeM*, 2008.

[26] "South African Band Re–planning Exercise–2^{nd} Edition," [Online] Available http://www.icasa.org.za, November, 2006.

[27] J. A. Lopez-Perez, "Detected Interferences at S–band from the 40–m Radiotelescope Servo Systems," Observatorio de Yebes, Instituto Geografico Nacional, Spain, VLBI 2010/ FRFF2009.

[28] R. P. Millenaar and H. J. Stiepel, "On self–generated RFI at Radio Astronomy Sites," Committee on Radio Astronomy frequencies, CRAF–04–1, 2003.

[29] "13.5m MeerKAT Dual Offset Antenna: System Description Document," VERTEX ANTENNENTECHNIK GmbH, 2013.

[30] P. C. Crane and L. Hillebrand, "Estimating Harmful Levels of Radio–Frequency Radiation, Light pollution, Radio interference, and Space Debris," *ASP Conference Series*, vol. 17, pp. 258–266, 2003.

[31] R. Oliva, E. Daganzo, Y. H. Kerr, S. Mecklenburg, S. Nieto, P. Richaume, and C. Gruhier, "SMOS Radio Frequency Interference Scenario: Status and Actions Taken to Improve the Environment in the 1400–1427–MHz passive band," Geoscience and Remote Sensing, IEEE Transactions, 2012.

[32] J. R. Fischer and C. Beaudet, "Sensitivity comparison of RFI monitor station and GBT L–band receiver," *Electronics Division Technical Note*, no. 209, 2007.

[33] P. Bolli, F. Gaudiomonte, F. Messina, R. Ambrosini, C. Bortolotti, and M. Roma, "The RFI monitoring systems for the Medicina and the Sardinia radio Telescopes," *In PoS RFI2010*, p. 29, 2010.

[34] G. C. Bower, "Radio Frequency Interference Mitigation," UC Berkeley Radio Astronomy Laboratory, IAU Working Group on Interference Mitigation.

[35] R. Ambrosini, "RFI Selection Criteria for Radio Telescopes," 17^{th} International Wroclaw Symposium and Exhibition on Electromagnetic Compatibility, 29 June – 1 July 2004.

[36] "Draft South African table of frequency allocations," ICASA, 2008.

[37] E. E. Rogers, "RFI shielding and mitigation techniques for a sensitive search for the 327 MHz line of Deuterium," M.I.T Haystack Observatory, 2007.

[38] J. Raza and A. J. Boonstra, "Spatial filtering of RF interference in radio astronomy," *IEEE Signal Processing Letters*, vol. 9, no. 2, pp. 64–67, 2002.

[39] G. M. Nita, D. Gary, Z. Liu, G. Hurford, and S. White, "Radio frequency interference excision using spectral–domain statistics," Publications of the Astronomical Society of the Pacific, 2007.

[40] "Report ITU–R RA.2126–1: Techniques for mitigation of radio frequency interference in radio astronomy," 2013.

[41] A. Gilloire and H. Sizun, "RFI mitigation of GNSS signals for radio astronomy: problems and current techniques," *Annals Telecommunications*, vol. 64, no. 9–10, pp. 625–638, 2009.

[42] M. Kesteven, "The current status of RFI mitigation in radio astronomy, Australia Telescope National Facility," CSIRO, 2009.

[43] P. G. Wiid, *Lightning Protection and Radio Frequency Interference Mitigation for the Karoo Array Telescope*. PhD thesis, Stellenbosch University, March 2010.

[44] P. S. van der Merwe, *Cabling and Interface for Karoo Array Telescope: Modelling and Metrology*. PhD thesis, Stellenbosch University, March 2011.

[45] P. G. Wiid and H. C. Reader, "Towards Electromagnetic Characterization of MeerKAT Telescope," URSI GASS, IEEE, Aug. 2014.

[46] B. K. Chung and H. T. Chuah, "Design and Construction of a Multipurpose Wideband Anechoic Chamber," *IEEE Antennas and Propagation Magazine*, vol. 45, Dec. 2003.

[47] C. A. Balanis, *Antenna theory, analysis and design*. Wiley, 3 ed., 2005.

[48] U. Jakobus and G. Smith, "State of the Art of Electromagnetic Modelling in FEKO," 6^{th} European Conference on Antennas and Propagation (EUCAP), 2011.

[49] D. B. Davidson, *Computational Electromagnetics for RF and Microwave Engineering*. Cambridge University Press, 2005.

[50] D. Ludick, E. Lezar, and U. Jakobus, "Characteristic Mode Analysis of Arbitrary Electromagnetic Structures using FEKO," IEEE, 2012.

[51] P. G. Wiid, "Lower Uncertainty PCB–LPDA Antenna Measurement on Open Area Test Site," IEEE, 2013.

[52] T. Williams, *EMC for Product Designers*. Newnes, ISBN: 0–7506–2466–3, 2 ed., 1996.

[53] C. Phillips, D. sicker, and D. Grunwald, "A Survey of Wireless Path Loss Prediction and Coverage Mapping Methods," *IEEE Communications Survey and Tutorials*, vol. 15, no. 1, 2013.

[54] T. J. Phiri, D. B. Davidson, and P. G. Wiid, "Propagation Modelling for the South African SKA Site," *IEEE*, 2015.

[55] J. S. Seybold, *Introduction to RF Propagation*. John Wiley & Sons, Inc., 2005.

APPENDIX A

MATLAB Program

A.1 Short Code for FSPL Verification

```
clear all;
close all;
clc;
%.....................................................................................

% load files
% Free Space loss and ground reflection (FEKO simulation)
FSP = importdata('Free_Space_SParameter1.s2p',' ',7); %path loss data
GR  = importdata('PEC_SParameter1.s2p',' ',7); %path loss and ground reflection data

Gain=importdata('Gain.dat','\t',1); %FEKO gain
gain=Gain.data(:,2);
%.....................................................................................

% CALCULATIONS
% .....................................................................................
F = FSP.data(:,1); %Frequency in GHz (check unit of your frequencies first)
F2=F/1e6;  %converting frequency to MHZ (check unit  of your frequencies)

S11_FSP = FSP.data(:,2).*exp(1i.*FSP.data(:,3).*pi/180);
S21_FSP = FSP.data(:,4).*exp(1i.*FSP.data(:,5).*pi/180);
S22_FSP = FSP.data(:,8).*exp(1i.*FSP.data(:,9).*pi/180);

S11_GP = GR.data(:,2).*exp(1i.*GR.data(:,3).*pi/180);
S21_GP = GR.data(:,4).*exp(1i.*GR.data(:,5).*pi/180);
```

```
S22_GP = GR.data(:,8).*exp(1i.*GR.data(:,9).*pi/180);

S21_FSP = abs(S21_FSP).^2./((1 - abs(S11_FSP).^2).*(1 - abs(S22_FSP).^2));
S21_GP = abs(S21_GP).^2./((1 - abs(S11_GP).^2).*(1 - abs(S22_GP).^2));

FSP=(1./S21_FSP).*(gain).^2; %ratio in power (invert S21_FSP for +ve values)
FSPL= 10*log10(FSP); %changing into dB

GR=(1./S21_GP).*(gain).^2;  %ratio in power (invert S21_GP for +ve values)
GP_FSPL=10*log10(GR); %changing into dB

%Free Space Path Loss Equation
%.....................................................................................
d=30;    %path length (m)
fspl = 20*log10(d) + 20*log10(F2) - 27.55; % f(MHz), d(m)

%PLOTS
%.....................................................................................

 figure;

 plot(F2,fspl,'b',F2, FSPL,'r',F2,GP_FSPL,'g');
 title('Path Loss Verification','FontWeight','bold','FontSize',14)
 xlabel('Frequency [MHz]','Fontsize',12), ylabel('FSPL/GR [dB]','Fontsize',12)

 hold on
 grid on
```

A.2 Computation for the Transfer Function

```
clear all;
close all;
clc;

% load files
% Free Space loss from FEKO simulation
FSP = importdata('Free_Space_SParameter1.s2p',' ',7);
 GP  = importdata('PEC_SParameter1.s2p',' ',7);


%FEKO Segment Currents in Amperes from (Plane wave 1v/m) ..........................
 sp = importdata('FSP_loss1.txt',',',1);
 sp1=sp.data(:,2);

 seg42 = importdata('Current_42_A.txt','\t',2);
 F1 = seg42.data(:,1);               %frequency in Hz
 current42= 1e6*seg42.data(:,2); %converting to uA
 R42=1./current42;               %Transfer function (TF)
 TF_seg42=20*log10(R42)-sp1;         %TF for seg 42 in dB

%  seg43 = importdata('Current_43_A.txt','\t',2);
%  current43= 1e6*seg43.data(:,2);
%  R43=1./current43;
```

```
%  TF_seg43=20*log10(R43)-sp1;

%  seg52 = importdata('Current_53.txt','\t',2);
% current52= 1e6*seg52.data(:,2);
%  R52=1./current52;
%  R52dB=20*log10(R52)-sp1;

 %On-site Currents in dBuA from (Plane wave ERS)..................................
 sdc_cl= importdata('Earth_SDC_Closed_dBuA.txt',',',2);
 sdc_current1= 10.^(sdc_cl.data(:,2)/20); %converting to uA


%  sdc_op= importdata('Earth-SDC_Open_dBuA.txt',',',2);
%  sdc_current2= 10.^(sdc_op.data(:,2)/20);
%
 lswitch= importdata('limit_switch_dBuA.txt',',',2);
 lcurrent= 10.^(lswitch.data(:,2)/20);
%
%  signal= importdata('signal_cable_dBuA.txt',',',2);
%  scurrent= 10.^(signal.data(:,2)/20);

%ERS E-field in dBuV/m.............................................
ers = importdata('ERS_field_Extrap_98_dBuV.txt','\t',1);
 F2 = ers.data(:,1); %frequency in MHz
field=  10.^((ers.data(:,2)-120)/20); %converting to V/m

% field=  10.^(ers.data(:,2)/20);
% CALCULATIONS
% ....................................................................
F = FSP.data(:,1);
S11_FSP = FSP.data(:,2).*exp(1i.*FSP.data(:,3).*pi/180);
S21_FSP = FSP.data(:,4).*exp(1i.*FSP.data(:,5).*pi/180);
S22_FSP = FSP.data(:,8).*exp(1i.*FSP.data(:,9).*pi/180);

%  S11_GP = GP.data(:,2).*exp(1i.*GP.data(:,3).*pi/180);
%  S21_GP = GP.data(:,4).*exp(1i.*GP.data(:,5).*pi/180);
%  S22_GP = GP.data(:,8).*exp(1i.*GP.data(:,9).*pi/180);

P21_FSP = abs(S21_FSP).^2./((1 - abs(S11_FSP).^2).*(1 - abs(S22_FSP).^2));
% P21_GP = abs(S21_GP).^2./((1 - abs(S11_GP).^2).*(1 - abs(S22_GP).^2));
 FSP=1./P21_FSP; %ratio in power (path loss)
 FSP_loss= 10*log10(FSP);

%  GP=1./P21_GP;
%  GP_loss=10*log10(GP);

d=30;    %path length (m)
fspl = 20*log10(d) + 20*log10(F2) - 27.55; % f(MHz), d(m)

loss=sqrt(FSP); %Power to E-field
received_field=field./loss; %removing the path loss

% Transfer function (v/m divide by uA)..............................

TFl=20*log10(received_field./lcurrent); % TF for limit switch in dB
% TFs=20*log10(received_field./scurrent);
```

```
% TF_op=20*log10(received_field./sdc_current2);
% TF_cl=20*log10(received_field./sdc_current1);

Fseg=F1/20*1e-6;           % Converting Segments Freq. to MHz

figure;
plot(F2, TF1,'b'); hold on
plot(F1/20*1e-6,TF_seg42,'r'); grid on
zoom on

%   S=[Fseg TF_seg42];
% S=[F2 20*log10(field)];

%   dlmwrite('I:\Line1\Line1\Last_Gasp\S81.txt',S);

%  figure;
%  plot(F2, FSP_loss,'b',F2, GP_loss,'r',F2,fspl,'g');% hold on
%  plot(F2,GP1,'r'); grid on
%  zoom on
% grid on;
% hold on;
% plot(F, 10*log10(1./P21_GP),'r');
```

APPENDIX B

Antenna Gain Calculations and Plots

B.1 Calculation for the Antenna Gains

By making use of Friis transmission formula in each of the three antennas, l_1, l_2 and l_{kat}, the following three equations can be defined (see chapter 3, section 3.2):

$$|S_{21\_l_1-l_2}|^2 = \frac{G_{l_1}G_{l_2}\lambda^2}{(4\pi R)^2} \tag{B.1}$$

$$|S_{21\_l_1-l_{kat}}|^2 = \frac{G_{l_1}G_{l_{kat}}\lambda^2}{(4\pi R)^2} \tag{B.2}$$

$$|S_{21\_l_2-l_{kat}}|^2 = \frac{G_{l_2}G_{l_{kat}}\lambda^2}{(4\pi R)^2} \tag{B.3}$$

The application of substitution method on the equations above, resulted into three equations that were used to uniquely calculate the gain functions for the antennas.

$$G_{l_1} = \frac{|S_{21\_l_1-l_2}||S_{21\_l_1-l_{kat}}|(4\pi R)}{|S_{21\_l_2-l_{kat}}|\lambda} \tag{B.4}$$

$$G_{l_2} = \frac{|S_{21\_l_1-l_2}||S_{21\_l_2-l_{kat}}|(4\pi R)}{|S_{21\_l_1-l_{kat}}|\lambda} \tag{B.5}$$

$$G_{l_{kat}} = \frac{|S_{21\_l_1-l_{kat}}||S_{21\_l_2-l_{kat}}|(4\pi R)}{|S_{21\_l_1-l_2}|\lambda} \tag{B.6}$$

B.2 Antenna Gain Functions

The gain functions for the LPDA antennas that were used to illuminate the MeerKAT scale model in the anechoic chamber were determined by using the three–antenna method described in subsection 2.7.2 of chapter 2 and the plots are shown in Figure B.1.

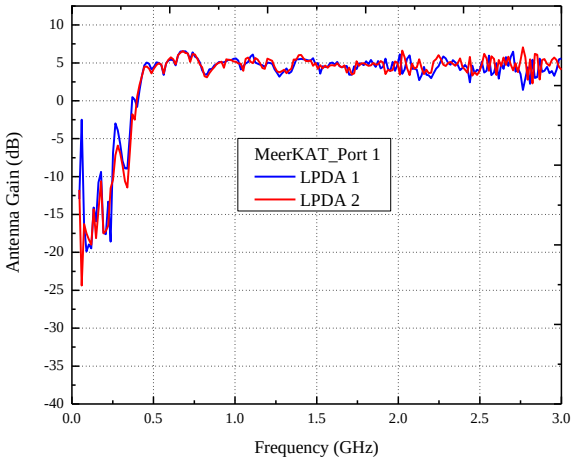

Figure B.1: LPDA antenna gain functions calculated using the three antenna–method. Only the values from the measurement were used in the calculations.

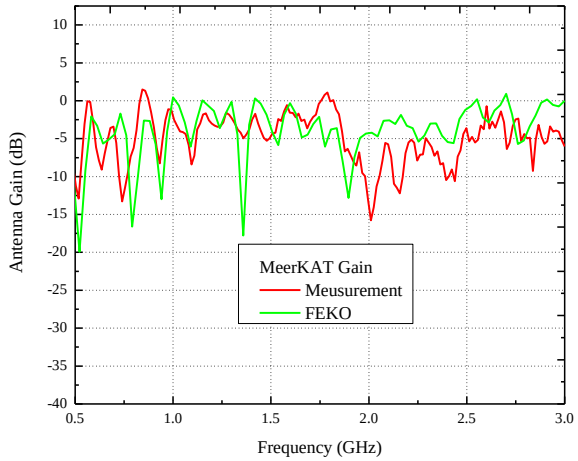

Figure B.2: Comparison of the gain functions calculated using the data from the measurement and simulation. The MeerKAT model is in a 90^0 orientation relative to the incoming plane wave.

These wideband LPDA antennas were designed at Stellenbosch University at the Department of Electrical and Electronic Engineering and they operate between 300 MHz to 10 GHz of frequency.

For the MeerKAT antenna, the gain functions were calculated from both the measurement and FEKO simulation results. The MeerKAT models were positioned in a ninety degree (90^0) angle of orientation relative to the incident plane wave as illustrated in Figure 3.3 (refer to chapter 3, section 3.2). The comparison between the measurement and the computational results are given in Figure B.2.

—And in the end it is not the years in your life that count, but the life in your years —

—Abraham Lincoln —